JGR Solid Earth

Key Points:

- A new model of South America mantle down to ~1,500 km was constructed with adjoint waveform tomography
- The cratonic nuclei are well resolved and, in the Amazonian Craton, higher-velocity anomalies correlate with the older provinces
- The Nazca Slab plunges into the lower mantle beneath northern South America and flattens toward the south near the 650 km discontinuity

Correspondence to:

C. Ciardelli,
caio.ciardelli@gmail.com

Author Contributions:

Data curation: Caio Ciardelli
Formal analysis: Caio Ciardelli, Marcelo Assumpção
Funding acquisition: Marcelo Assumpção
Investigation: Caio Ciardelli, Marcelo Assumpção
Methodology: Caio Ciardelli, Ebru Bozdağ
Project Administration: Marcelo Assumpção
Resources: Marcelo Assumpção, Suzan Lee
Software: Caio Ciardelli, Ebru Bozdağ
Supervision: Marcelo Assumpção, Ebru Bozdağ, Suzan Lee
Validation: Caio Ciardelli
Visualization: Caio Ciardelli, Marcelo Assumpção

Adjoint Waveform Tomography of South America

Caio Ciardelli[1] , Marcelo Assumpção[1] , Ebru Bozdağ[2] , and Suzan van der Lee[3]

[1]Department of Geophysics, Institute of Astronomy, Geophysics and Atmospheric Sciences, University of São Paulo, São Paulo, Brazil, [2]Department of Geophysics, Colorado School of Mines, Golden, CO, USA, [3]Department of Earth and Planetary Sciences Weinberg College of Arts and Sciences, Northwestern University, Evanston, IL, USA

Abstract We used 3D spectral-element seismic wave simulations and data from 112 earthquakes and 1,311 seismic stations, totaling 20,884 unique ray paths, to construct an adjoint waveform tomographic model of South America. We performed 23 conjugate-gradient iterations using exponentiated phase (EP) measurements. Our final model (SAAM23, South American Adjoint Model—iteration 23) shows a 50% decrease in the EP misfit relative to its 3D starting model. We further assessed the phase misfit reduction by using cross-correlation travel-time measurements of 53 earthquakes not included in the inversion. We estimated SAAM23 resolution using point-spread function tests and density coverage analysis. The Nazca Slab is well imaged and is shown to be continuous in the 300–500 km depth range. Beneath northern South America, the slab traverses the mantle transition zone and continues into the lower mantle. In the central and southern part of South America, the slab appears to flatten near the 650 km discontinuity before continuing into the lower mantle. In the stable Precambrian platform, both cratons (Amazonian and São Francisco), as well as covered cratonic blocks beneath the intracratonic Paraná and Parnaíba basins (Paranapanema and Parnaíba, respectively), show high velocities at lithospheric depths. The seismic Lithosphere/Asthenosphere boundary (LAB) agrees well with published values obtained by *S*-wave receiver functions. In the Amazonian craton, the positive lithospheric *S*-wave velocity anomalies and LAB depth increase with the average age of the geochronological provinces. No lithospheric high-velocity anomalies were found beneath the Río de la Plata Craton.

Plain Language Summary We developed a new model of mantle seismic velocities beneath the South American Plate using adjoint waveform tomography by calculating synthetic seismograms that match observations from 112 earthquakes and 1,311 stations. This model (SAAM23, South American Adjoint Model—iteration 23) was validated with an independent set of observations. The model shows the Nazca Slab crossing the 410 and 650 km seismic discontinuities and plunging directly into the lower mantle. In the southern part of the continent, the Nazca Slab flattens and remains close to the 650 km discontinuity. The oldest continental regions (the Amazonian and São Francisco cratons, as well as the cratonic blocks buried beneath the Paraná and Parnaíba basins) have high velocities in the upper mantle. The boundary between the lithosphere (the rigid upper portion of the mantle) and the asthenosphere (the more ductile region below), called LAB, estimated by SAAM23 agrees well with other studies. In the Amazonian Craton, both the upper mantle velocities as well as the LAB depth increase with the average age of the geochronological provinces. However, no high velocities were found beneath the Río de la Plata Craton.

1. Introduction

The seismic structure of the South American mantle, especially beneath the stable continental interior, has not been studied on a regional scale, with limitations in heterogeneous resolving power caused mainly by a dearth of seismographic stations outside the Andes Mountains. The continent is composed of three main tectonic domains (Figure 1: the Archean-Proterozoic South American Platform, the Phanerozoic Patagonian Platform, and the active Andean Belt. The stable platforms are composed of several cratons and cratonic blocks (Figure 1) amalgamated in the Neoproterozoic to form the Gondwana supercontinent. In this stable interior, several regional scale tomographic studies using teleseismic *P* and *S* waves (e.g., Affonso et al., 2021; Assumpçao et al., 2004; Costa et al., 2020; Rocha, Assumpção, et al., 2019; Rocha, Azevedo, et al., 2019; Rocha et al., 2011; Schimmel et al., 2003; Simões Neto et al., 2019; VanDecar et al., 1995) have delimited the lateral extension of those lithospheric blocks and how they were affected by Mesozoic and Cenozoic intraplate magmatism. However, with the available station density in South America, teleseismic tomography models do not usually have enough vertical resolution to define the lithospheric thickness. On the other hand, regional and continental-scale surface-wave

Writing – original draft: Caio Ciardelli,
Marcelo Assumpção
Writing – review & editing: Ebru
Bozdağ, Suzan Lee

tomography (e.g., Feng et al., 2004; Heintz et al., 2005; Rosa et al., 2016; Van der Lee et al., 2001) has better vertical resolution down to about 300 km and provides better estimates of lithospheric thicknesses. Surface-wave tomography has identified the deepest lithosphere in the oldest units of the Amazonian Craton (AC) and the southern part of the São Francisco Craton (SFC; Figure 1). However, due to the lower lateral resolution, compared to body-wave tomography, smaller lithospheric blocks have not been identified in a consistent way. Feng et al. (2007) and Celli et al. (2020) using partitioned waveform inversion (PWI; Nolet, 1990) and automated multimode inversion (AMI; Lebedev et al., 2005), respectively, better resolved the cratonic nuclei by inverting surface- and *S*-wave waveforms simultaneously.

In the Andes, continental-scale teleseismic *P*- and *S*-wave tomographic models (e.g., Portner et al., 2020; Rodríguez et al., 2021) have mapped the geometry of the subducting Nazca Slab below the Andes. However, some structural features are still controversial, such as the continuity of the slab at depths beyond the stagnant segment near the Peruvian Andes (Mohammadzaheri et al., 2021), or the geometry of the slab in the mantle transition zone. Beneath the AC (north of ∼20°S) global tomography models (Hosseini et al., 2020; Lei et al., 2020; Obayashi et al., 2013; Simmons et al., 2012) as well as continental models (Portner et al., 2020; Rodríguez et al., 2021) tend to show the Nazca Slab plunging directly into the lower mantle. In the southern part of South America, on the other hand, the above models do not show a consistent position of the subducting Nazca Slab, which sometimes appears to be stagnant within the mantle transition zone (MTZ) and sometimes below it.

The recent installation of the Brazilian permanent network (Bianchi et al., 2018) and several temporary deployments (e.g., Rivadeneyra-Vera et al., 2019) have enabled better seismic recording coverage of the plate's tectonically stable interior, which help increase the resolution of tomographic images of the region. In this study, using the available seismic data, we performed adjoint waveform tomography (or "adjoint tomography"; Fichtner et al., 2006; Tape et al., 2007; Tarantola, 1984; Tromp et al., 2005), an iterative full-waveform inversion (FWI) technique, incorporating 3D numerical wave simulations in structural inversions to construct new *P*- and *S*- wave velocity models of South America. Adjoint tomography has so far been successfully applied in regional (e.g., Tape et al., 2009), continental (e.g., Fichtner et al., 2009; Zhu et al., 2015) and global (Bozdağ et al., 2016; Lei et al., 2020) scale studies and uses more information than classical body-wave travel-time and surface-wave phase/group velocity methods and the multi-mode PWI and AMI methods, thus improving lateral as well as vertical resolving power.

We calculated the wave propagation and data sensitivity kernels in 3D background models using spectral-element seismic wave simulations by the SPECFEM3D_GLOBE package (Komatitsch & Tromp, 1999, 2002a, 2002b; Komatitsch & Vilotte, 1998). We used the exponentiated phase (EP) misfit (Yuan et al., 2020), an instantaneous phase measurement (Bozdağ et al., 2011), to fit the phase information of body- and surface-waves and constructed our model by performing 23 conjugate-gradient iterations.

In the following, we first describe the geology of South America and give information about how we performed our adjoint tomography in Sections 2 and 3, respectively. In Section 4, we assess the quality of our model. In Section 5, we present SAAM23 and interpret our observations in the study region's geological and tectonic context. We also compare SAAM23 to published tomographic models. Finally, in Section 6, we summarize our results and present our findings.

2. South America Geological Provinces

The South American continent includes Archean cratons and sedimentary rock-covered Proterozoic platforms (so-called South American Platform), the Paleozoic orogenies of the Patagonia Platform, and Mesozoic-Cenozoic deformation related to the active mountain building and volcanism in the Andean Belt (Figure 1). Here we summarize the most important tectonic and geological aspects of these three main domains.

2.1. South American Platform

The South American Platform is defined as the tectonically stable continental area not affected by Phanerozoic orogenies such as the Andean and Caribbean orogenies. This area has two main domains (de Almeida et al., 2000): the Amazonian Domain (AD) and the Brasiliano Domain (BD), approximately separated by the Transbrasiliano Lineament (TBL; Chamani, 2020) and the Araguaia Fold Belt (AFB), as shown in Figure 1.
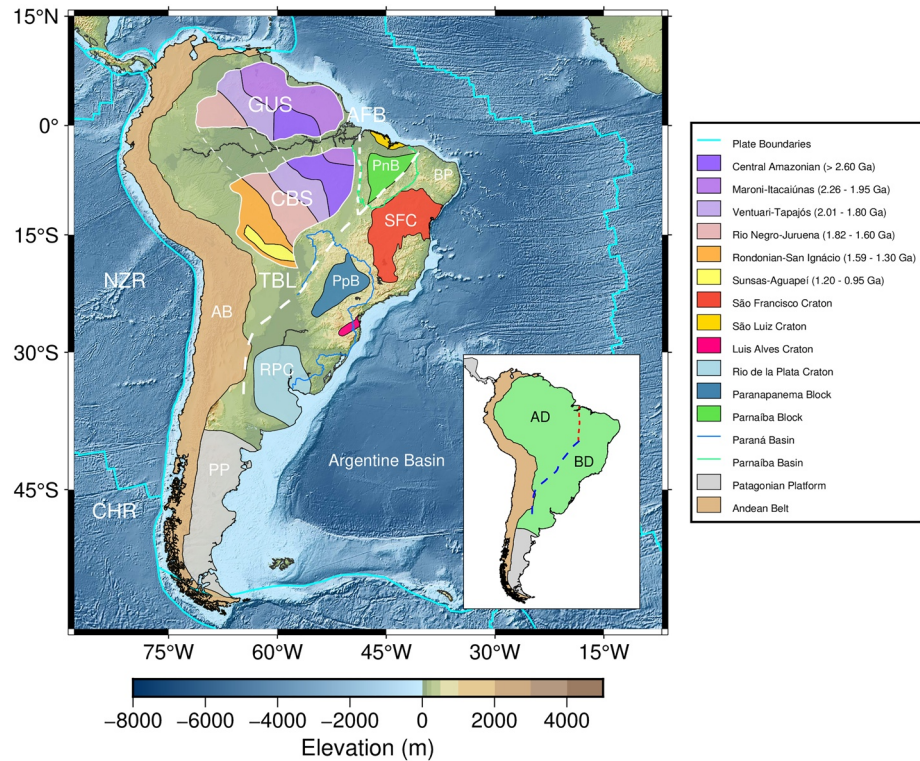
Figure 1. Major geological structures in South America. The Andean Belt (AB) appears in light brown and the Patagonian Platform (PP) in light gray. The cratons are represented by all the other colored polygons. The Amazonian Craton is composed of the Guyana Shield (GUS) to the north and the Central Brazil Shield (CBS) to the south. We also show the six geochronological provinces: Central Amazonian, Maroni-Itacaiúnas, Ventuari-Tapajós, Rio Negro-Juruena, Rondonian-San Ignácio, and Sunsas-Aguapeí. The darkblue polygon is the Paranapanema Block (PpB) and the lightgreen the Paranaíba Block (PnB). The map also includes the Paraná (blue contour) and the Parnaíba (green contour) basins, the Transbrasiliano Lineament (TBL) and the Araguaia Fold Belt (AFB). BP, NZR, and CHR are the Borborema Province, the Nazca Ridge and the Chile Ridge, respectively. Inset map: South American Platform (light green), Patagonian Platform (light gray), and Andean Belt (light brown). The Amazonian Domain (AD) is separated from the Brasiliano Domain (BD) by the TBL in the southern and central parts of Brazil, and possibly by the AFB in the north.

The AD includes the AC, which comprises several large terranes that formed in the Archean to Neoproterozoic eons. These terranes are exposed in the Guyana and Central Brazil shields and overlain by the Paleozoic Amazon Basin (de Almeida et al., 2000; COUTINHO, Maria Glícia da Nóbrega, 2008) elsewhere. Teixeira et al. (1989), Tassinari and Macambira (1999), and Cordani et al. (2016) separate the AC into six geochronological provinces (Figure 1). The AC began as an Archean protocraton (Central Amazonian Province, >2.3 Ga) and had several terranes accreted via orogenic belts and magmatic arcs (Maroni-Itacaiúnas, 2.2–1.95 Ga; Ventuari-Tapajós, 1.95–1.8 Ga; Rio Negro-Juruena, 1.8–1.55 Ga; Rondonian-San Ignácio, 1.5–1.3 Ga; and Sunsas-Aguapeí, 1.25–1.0 Ga), eventually colliding with Laurentia (de Brito Neves & Fuck, 2014). Although Santos et al. (2000), Santos (2003), and Vasquez et al. (2008) prefer different boundaries for these geochronological provinces, both geochronological models show the same trend of younger ages toward the west.

Surface-wave tomography models (Celli et al., 2020; Feng et al., 2007; Heintz et al., 2005) generally show high lithospheric velocities in the eastern part of the AC (beneath the oldest provinces of Central Amazon, Maroni-Itacaiúnas, and Ventuari-Tapajos) compared to the younger western provinces. Feng et al. (2007) found lithospheric thicknesses up to ~200 km beneath the oldest Central Amazonian Province, including beneath the western part of the Amazon Basin, but found no correlation between the distribution of high lithospheric velocity anomalies and the smaller geochronological provinces. Heintz et al. (2005) and Celli et al. (2020) found similar lithospheric velocities as well as waning lithospheric velocities beneath the Amazon Basin.

The BD is comprised of the large SFC, as described by Heilbron et al. (2016) and references therein, and several other smaller cratonic fragments, some of which (Parnaíba and Paranapanema blocks, and part of the Río de

la Plata Craton) inferred to lie beneath intracratonic basins, as shown in Figure 1. Archean to Paleoproterozoic rocks are exposed in the northeast and the south of the SFC. These cratons and cratonic blocks were amalgamated during the assembly of Gondwana, together with the AC (de Almeida et al., 2000; de Brito Neves & Fuck, 2014; Cordani & Teixeira, 2007; Cordani, Teixeira, et al., 2009; Teixeira et al., 2020).

Global tomography models, such as CAM16 (Priestley et al., 2018) or GLAD-M25 (Lei et al., 2020) do not usually show separate high-velocity anomalies for the AC and the SFC, but continental scale tomography models (Celli et al., 2020; Feng et al., 2007; Heintz et al., 2005) do. However, the SFC is not always distinguished from the smaller neighboring blocks. Clearly, although there is general agreement among regional tomography models regarding the high-velocity lithosphere of the two domains of the South American Platform, smaller blocks and cratons have not yet been consistently delineated.

2.2. Patagonian Platform

The Patagonian Platform, the portion of the stable South American continent south of 35°S (Figure 1), is younger in age and was involved in Phanerozoic orogenic processes (de Almeida et al., 2000). According to Ramos (2004), Patagonia is composed of allochthonous terranes that joined Gondwana in the Early Permian. This younger age is reflected in low upper-mantle velocities seen in both global (e.g., Lei et al., 2020; Priestley et al., 2018) and continental scale surface-wave tomography models (Celli et al., 2020; Feng et al., 2007; Heintz et al., 2005).

### 2.3. Andean Belt and Nazca Plate

The Andes Mountain Belt, the second highest orogenic belt on Earth, were generated by the Cenozoic tectonic shortening of the South American Plate margin overriding the subducting Nazca Plate (e.g., Ramos, 1999; Sobolev & Babeyko, 2005). Along the Andean Belt (Figure 1), there are several cordilleras, sierras, plateaus, basins, and valleys (Cordani et al., 2000). Formation of the Andes began in the late Cretaceous with subduction of the Farallon Plate beneath the northern part of the continent, propagating to the southern portion of the Andes by the early Paleogene (e.g., Chen et al., 2019).

The Andean subduction zone is one of the most tectonically and seismically active on Earth. The convergence of the Nazca and the South American plates caused the uplift of the Andes and also created a volcanic chain along the whole mountain belt. The seismicity and volcanic activity along the western edge of South America vary significantly as a result of complex geological processes (Hayes et al., 2015) caused by spatial and temporal changes in the dip angle (Ramos, 1999) of the subducting Nazca Slab. At present, the subducting Nazca Slab has three relatively flat slab segments (Figure 2): the Colombian Flat Slab (from 8°N to 5°N), the Peruvian Flat Slab (from 3°S to 15°S), and the Pampean Flat Slab in Argentina (25°S to 32°S). The two largest flat segments (Peruvian and Pampean), are imaged at about 100–150 km depth by surface-wave tomography models (e.g., Celli et al., 2020; Feng et al., 2007; Heintz et al., 2005).

Earthquakes in South America are typically shallower than 300 km or deeper than 500 km. The deep earthquakes concentrate in two zones: one that runs beneath the Peru-Brazil border and another that extends from central Bolivia to central Argentina (Hayes et al., 2015). The slab geometry presented by Hayes et al. (2018; Figure 2) interpolated earthquake gaps by using seismic-tomographic models. However, some tomographic models suggest gaps in the subducting Nazca Slab, such as downdip from the Peruvian Flat Slab (e.g., Mohammadzaheri et al., 2021).

3. Adjoint Tomography

The resolution of seismic-tomographic models is directly controlled by data coverage and the chosen forward and inverse theory used in tomography. Seismic tomography is traditionally based on ray theory, which is a high-frequency approximation (Cervenỳ, 2001). Since the current resolution of seismic tomography has reached the limits of ray theory (Peter et al., 2009) finite-frequency effects (e.g., Dahlen et al., 2000) have been taken into account both in body-wave (e.g., Montelli et al., 2004) and surface-wave (e.g., Zhou et al., 2006) tomographic studies computing Fréchet kernels in 1D reference models. Advances in numerical methods and computational power have enabled to solve the wave equation numerically by taking the full complexity of the medium and source into account. Lekić and Romanowicz (2011) and French and Romanowicz (2015) used 3D
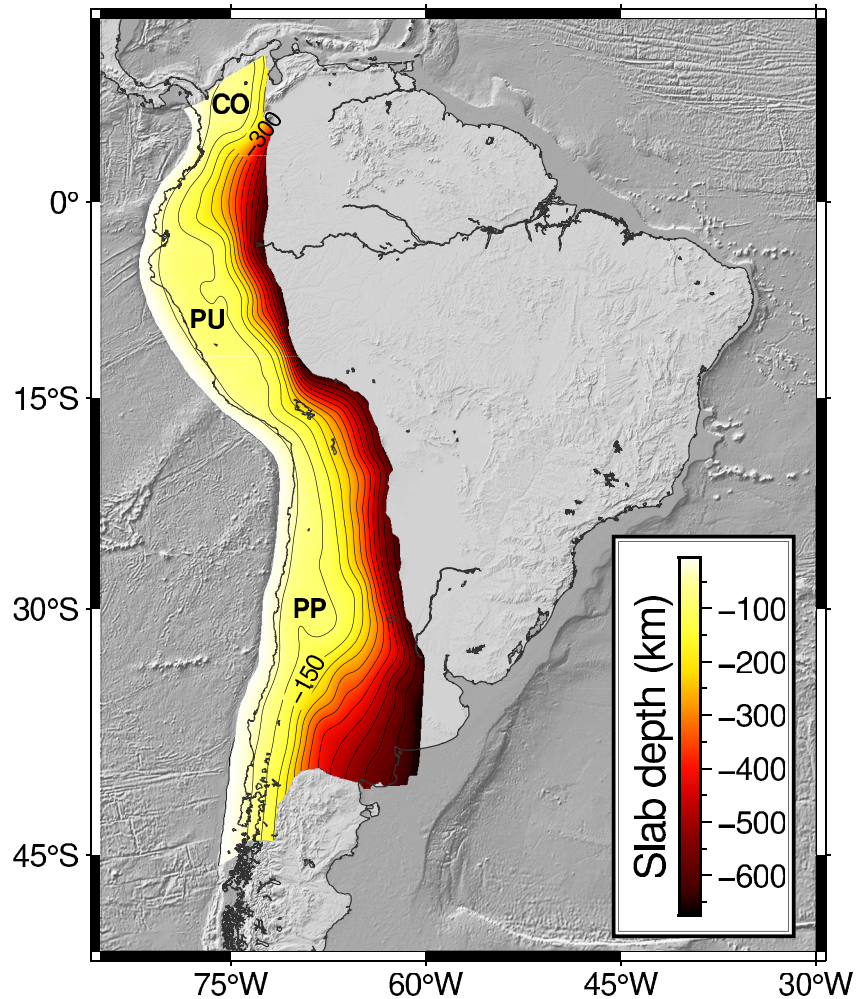
Figure 2. Representation of the Nazca Plate based on the Slab2 model. Contours are plotted at every 50 km. The subducting Nazca Slab is relatively horizontal beneath northern Colombia (CO), Peru (PU), and western Argentina (Pampean Flat Slab, PP), as shown by the far eastern 150 km depth contour.

spectral-element wave simulations (Capdeville et al., 2003; Chaljub et al., 2003; Chaljub & Valette, 2004; Komatitsch & Tromp, 1999, 2002a, 2002b; Komatitsch & Vilotte, 1998; Peter et al., 2011) combined with kernels derived using non-linear asymptotic coupling theory (NACT; Li & Romanowicz, 1995, 1996) in waveform inversions. Today's computational resources have enabled us also to compute 3D data sensitivity kernels (so called Fréchet kernels) numerically in 3D background models in full-waveform inversions based on the adjoint method.

Introduced by Tarantola (1984) into seismology, the adjoint tomography takes advantage of the full complexity of the seismic wavefield both in the computation of synthetic seismograms and Fréchet kernels (using the adjoint-state method) to iteratively update seismic-tomographic models (Fichtner et al., 2006; Plessix, 2006; Tromp et al., 2005; Virieux & Operto, 2009). 3D waveform simulations allow for maximizing the information extracted from each seismic record with appropriately defined misfit functions based on the difference between observed and simulated (synthetic) data (e.g., Bozdağ et al., 2011; Brossier et al., 2010). A review of methods, including a discussion of the tomographic resolution of the mantle models, may be found in Liu and Gu (2012).

In this study, we provide new constraints on geological and tectonic processes in South America by constructing new *P*- and *S*-wave velocity models based on adjoint tomography. At this stage, we use the phase information measured by comparing observed and synthetic waveforms only excluding the amplitude information of waveforms to simplify the inverse problem and focus on the elastic structure. We used the SPECFEM3D_GLOBE
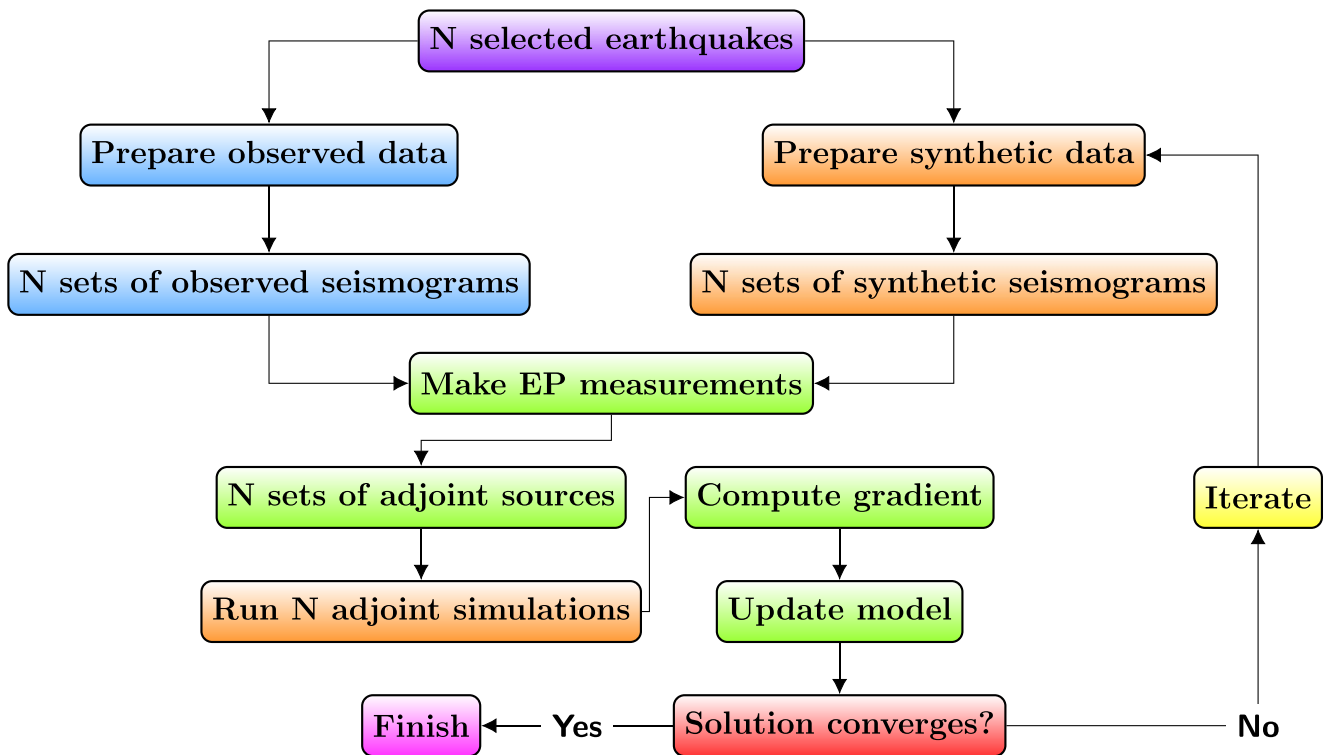
Figure 3. Adjoint tomography workflow. The preparation of the observed data stage comprises both the data request as well as the pre-processing: detrend, taper, remove response, filter, and downsample. The preparation of the synthetic data consists in running the mesher and the N forward simulations using the CMT source files. The measurement stage includes the selection of windows, the misfit measurements, and the computation of the adjoint sources. This is the stage in which our workflow differentiates from others (e.g., Bozdağ et al., 2016; Lei et al., 2020) as we used our own window selection algorithm, designed to create large windows, which are adequate for EP measurements (Yuan et al., 2020). The window selection and the creation of the adjoint sources were carried out using PyWinAdjoint. The adjoint sources must be re-computed every iteration whereas we kept the windows fixed over a range of iterations (Figure 7). The computation of gradient comprises the summation of all kernels, smoothing, and preconditioning. Lastly, the model update stage includes the determination of the step length and the model update using the conjugate gradient method.

package (Komatitsch & Tromp, 2002a, 2002b) to perform both forward (to compute synthetic seismograms) and adjoint simulations (to compute the gradient of our misfit function using the adjoint-state method).

Our tomography workflow has three basic stages (numerical simulations, pre-processing, and post-processing) which closely follow Zhu et al. (2012) and Bozdağ et al. (2016), except the pre-processing part (Figure 3). The pre-processing stage involves selection of measurement windows and computation of adjoint sources where we used the EP misfit (Yuan et al., 2020), an instantaneous-phase misfit (Bozdağ et al., 2011), for our phase measurements instead of frequency-dependent cross-correlation travel-times used in Zhu et al. (2012), Bozdağ et al. (2016), and (Lei et al., 2020). For the selection of measurement windows, we used our Python-based window-selection algorithm, PyWinAdjoint (Ciardelli, 2021) which is similar to the automated window selection algorithm FLEXWIN (Maggi et al., 2009). In the post-processing stage we updated the model iteratively based on a conjugate-gradient optimization method (Fletcher & Reeves, 1964; Nocedal & Wright, 2006). This section first gives information about our starting model and forward and adjoint simulations, then pre- and post-processing stages.

3.1. Starting Model and Model Parametrization

Our starting model M00 is a combination of the 3D mantle model S362ANI (Kustowski et al., 2008) and the 3D global crustal model CRUST1.0 (Laske et al., 2012). S362ANI is radially anisotropic in the uppermost mantle and was inferred from a compilation of surface-wave phase velocities, long-period waveforms, and body-wave travel times. S362ANI includes topography of the 410 and 650 km discontinuities in the upper mantle. CRUST1.0

is global crustal model compiled from crustal thickness estimates inferred from active-source seismic and passive source receiver function studies as well as global data on sedimentary layers, with a resolution of a $1° \times 1°$.

Following the starting model S362ANI + CRUST1.0, our model parameterization includes transverse isotropy in the upper mantle while the rest of the model is isotropic. We made this choice because our data coverage decreases considerably below 800 km depth (Figure S8 in Supporting Information S1), hampering adequate resolution for anisotropy.

Following Zhu et al. (2012) and Bozdağ et al. (2016), we reduced the redundant dependency of P and S-wave velocities on the shear modulus by ignoring P-wave anisotropy and inverting for the bulk sound velocity c ($c = \sqrt{\kappa/\rho}$ where κ is the bulk modulus and ρ is the density).

The trade-off between density and wave velocities is a well-known problem. Some researchers address it by attempting to simultaneously invert wave velocities and density (e.g., Beller et al., 2018; Blom et al., 2020). To minimize the trade-off between parameters, we preferred to scale the density from the updated shear-wave velocity model at each iteration similar to Zhu et al. (2012) and Bozdağ et al. (2016). Following Montagner and Anderson (1989), we used the following relation to scale density:

$$\delta \ln \rho = 0.33\, \delta \ln \beta, \tag{1}$$

where β is the isotropic shear wave velocity estimated via the Voigt average (Babuska & Cara, 1991):

$$\beta = \sqrt{\frac{2\beta_v^2 + \beta_h^2}{3}}. \tag{2}$$

Then, we have four parameters in our inversion: bulk-sound velocity c, vertically polarized shear-wave velocity (β_v), horizontally polarized shear-wave velocity (β_h), and the dimensionless parameter η (Kawakatsu, 2016). The gradient of our misfit function, which is discussed in Section 3.2.3, may be written as:

$$\delta \chi = \int_V \left(K_c\, \delta \ln c + K_{\beta_v}\, \delta \ln \beta_v + K_{\beta_h}\, \delta \ln \beta_h + K_\eta\, \delta \ln \eta \right)\, dV, \tag{3}$$

where K_c, K_{β_v}, K_{β_h}, and K_{β_η} are the Fréchet derivatives of c, β_v, β_h, and η parameters, respectively, and the logarithmic terms are the associated model perturbations.

3.2. Forward Simulations and the Pre-Processing Stage

We used the 3D global wave propagation solver SPECFEM3D_GLOBE package in forward and adjoint simulations. Our study region fits to $90° \times 90°$ one chunk (the globe consists of six chunks in the solver). Topography, bathymetry, gravity (the Cowling approximation; Cowling, 1941), ellipticity, rotation, the ocean load, and attenuation were taken into account during numerical simulations. The details of our numerical simulations (i.e., absorbing boundaries, the mesh, etc.) are given in the Supporting Information S1. In the following, we discuss the pre-processing stage to compute adjoint sources for adjoint simulations.

3.2.1. Data Selection

In this study, we used seismic data from 112 earthquakes (Figure 4a) selected from the global CMT (Centroid Moment Tensor) catalog (Dziewonski et al., 1981; Ekström et al., 2012) from April 1994 to April 2018, with moment magnitudes (M_w) between 6 and 7. This M_w range was selected from a larger list of 270 earthquakes ($M_w > 5.5$). Since numerical wave simulations are performed for each earthquake, we tried to optimize the cost of simulations by selecting events with high-quality data while trying to preserve a good azimuthal coverage. We also used as many stations as possible, given that the number of receivers does not change the computational cost of simulations. The mesher does not use the actual stations' elevations, placing all of them at the averaged topography values from ETOPO1. We also excluded events larger than $M_w = 7$ where finite-source effects become significant considering the minimum period of our simulations (17 s). We downloaded the observed data from both permanent and temporary networks, including stations from USP, IRIS, and GFZ (see the complete list in Section 7). The events were selected by checking the similarity between observed and synthetic waveforms. Before performing a quality check, observed and synthetic waveforms went through classical data processing
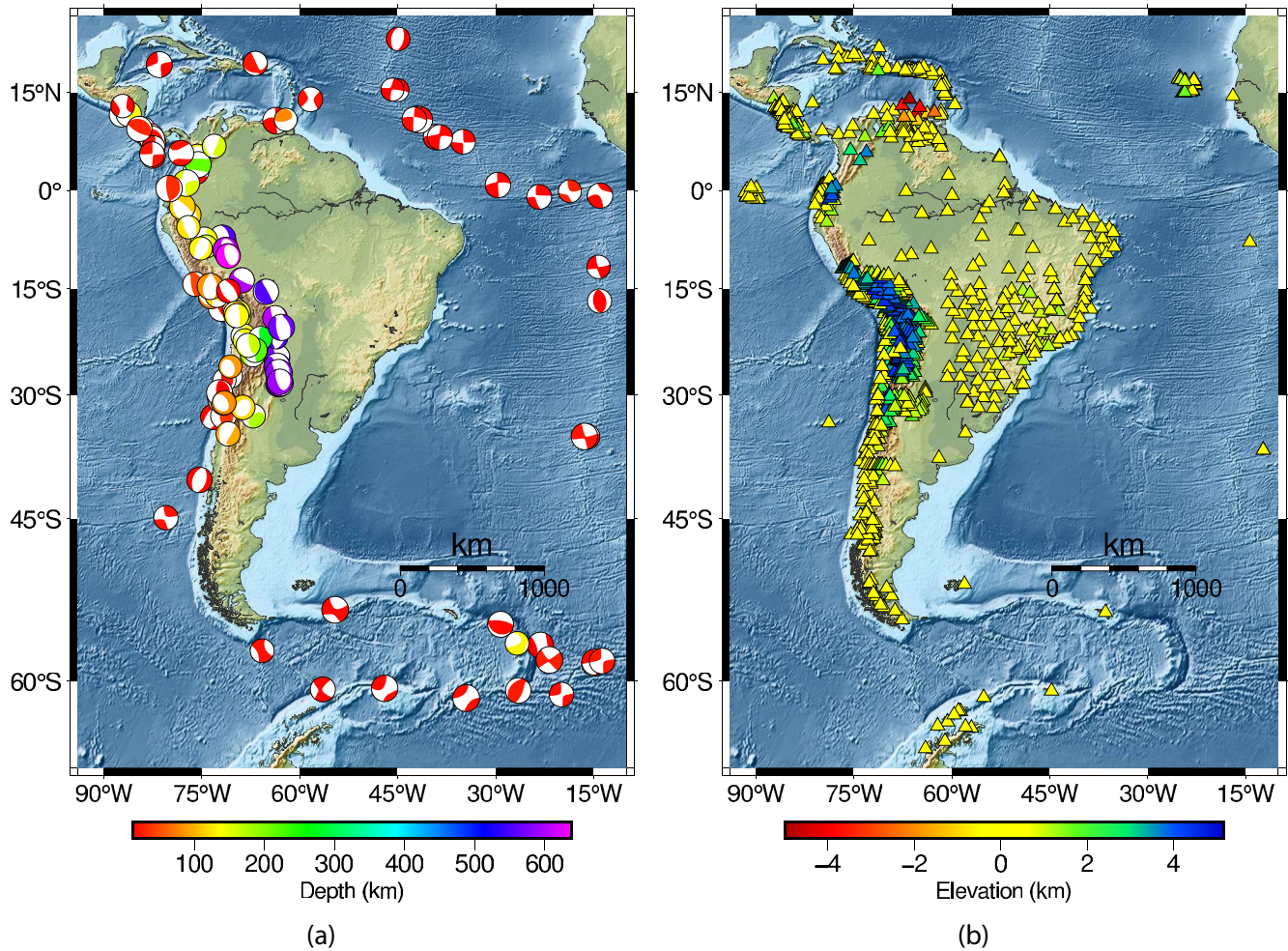
Figure 4. (a) The 112 selected earthquakes. The earthquakes' focal mechanisms are plotted as beach balls and their color indicates hypocentral depth. (b) The 1,311 selected stations, colored by elevation.

steps, that is, removing the mean and trend, tapering, and low-pass filtering. The same data processing steps and filters were applied to both observed and synthetic seismograms. The observed waveforms were additionally deconvolved with the instrument's response to ground displacement.

After computing synthetic ground displacement seismograms, we visually compared them to observed ones. Some receivers appeared to have orientation issues, such as swapped signal polarities and swapped horizontal components. In such cases, we corrected the metadata information when we could do so reliably or discarded the data. We also excluded waveforms with large discrepancies between observed and synthetic amplitudes (Figure 5). After this visual inspection and manual cleaning, we kept data from 1,311 stations. Figure 4 shows the distribution of sources and receivers used in this study.

3.2.2. Measurement Window Selection

We further checked the quality of waveforms and select measurement windows using our Python-based window selection algorithm, PyWinAdjoint. PyWinAdjoint utilizes fewer selection parameters than FLEXWIN (Maggi et al., 2009), but has extra parameters designed for quality control purposes, such as eliminating problematic data before the inversion (Section 7). PyWinAdjoint uses a four-stage algorithm, in which the first three steps detect and reject noisy data (Figure 5a). The last step carries out the time-window selection based on waveform and amplitude similarity. Before selecting measurement windows, we processed observed and synthetic data in three-period bands. Figure 5 illustrates the three-period bands used in this study: 17–45 s (Figure 5b), 30–60 s (Figure 5c), and 45–100 s (Figure 5d).
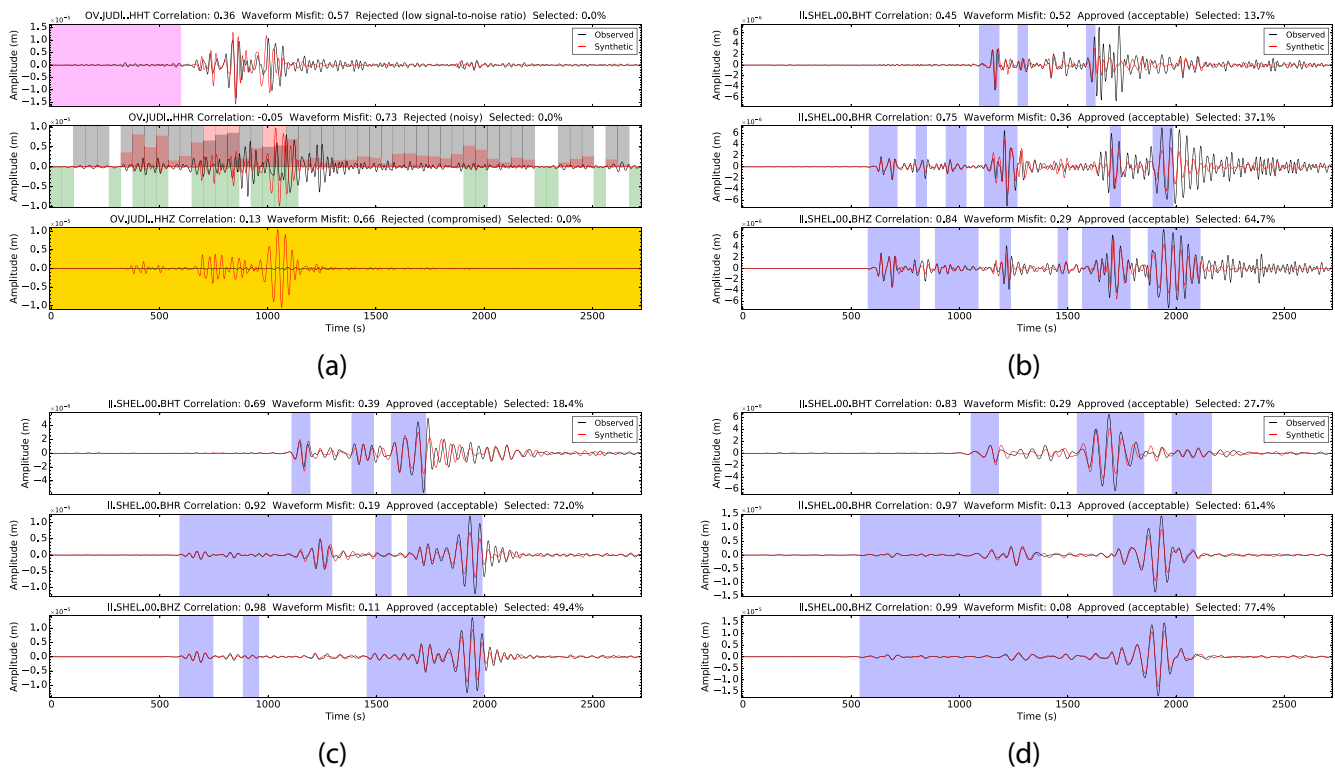
Figure 5. (a) Automated detection and removal of noisy or compromised data. Compromised or noisy seismograms are identified by: (1) Highly different overall amplitudes [Z-component of (a), marked in yellow]; (2) Large amplitude signal before *P*-wave arrival [T-component of (a). The trace segment used to calculate the signal-to-noise ratio is marked in magenta]; (3) Amplitude differences that exceed a certain threshold in more than 20% of the record duration (R-component of (a)]. The algorithm splits the trace into 50 segments and, for each of them, averages the absolute values of the signal both for the observed and the synthetic seismograms. If the ratio between these two numbers exceeds 0.35, the segment is rejected. Accepted segments appear in green. If more than 10 segments are rejected, the whole component is discarded. Red and gray bars show the amplitude ratios). (b) Selected windows in the 17–45 s period band. (c) Selected windows in the 30–60 s period band. (d) Selected windows in the 40–100 s period band. The algorithm only selects windows after the *P*-wave arrival detected at the synthetic seismogram.

3.2.3. Measurements and the Computation of Adjoint Sources

The choice of the misfit function is a key step that affects the success and the convergence of FWI (e.g., Modrak & Tromp, 2016). It is common to split seismic traces into smaller measurement windows using window-selection algorithms (e.g., Chen et al., 2017; Lee & Chen, 2013; Maggi et al., 2009) to select high-quality portions of seismograms and maximize the information extracted from each time series. Both time-domain cross-correlation (Dahlen et al., 2000; Luo & Schuster, 1991; Marquering et al., 1999; Tanimoto, 1995; Tromp et al., 2005) and frequency-dependent multitaper cross-correlation (Tape et al., 2009; Zhou et al., 2004, 2005) measurements tend to highlight the maximum amplitude signals in measurement windows where scattered waves, which provide valuable constraints on the structure of the medium they propagate through, are generally suppressed (e.g., Rickers et al., 2012). Unlike cross-correlation measurements, time-frequency misfits (e.g., Fichtner et al., 2009; Kristeková et al., 2009) or instantaneous phase and envelope misfits (e.g., Bozdağ et al., 2011) can be applied to wave trains without the need for smaller measurement windows (Rickers et al., 2013). used an instantaneous phase misfit to image the Icelandic plume to overcome potential wavefront-healing problems (e.g., Nolet & Dahlen, 2000). In a synthetic study, Yuan et al. (2020) proposed the EP misfit, a variant of the instantaneous phase measurement of Bozdağ et al. (2011), to alleviate the phase wrapping problem.

The last stage of the pre-processing is the computation of adjoint sources based on the chosen misfit function. We chose the EP misfit for three reasons: (a) We tried to linearize the inverse problem focusing on the elastic parameters, which are more linearly related to the phase information; (b) EP measurements can be applied to wave trains, which do not require as many time windows as cross-correlation measurements need and highlight smaller amplitude signals in the total gradient better; (c) EP deals with the cycle skip problem better than IP measurements by tapering phase shifts larger than $\pi/4$. Since the EP misfit (Equation 4) shows non-convexity at large

phase difference (Yuan et al., 2020), appropriate window selections are still necessary to mitigate the cycle-skip problem and make sure to select portions of seismograms with high data quality.

Following Yuan et al. (2020), we define the EP misfit based on the observed $\tilde{d}(t)$ and synthetic $\tilde{s}(t)$ analytic signals normalized by their envelopes:

$$\chi_{EP} = \frac{1}{2} \sum_{s,r} \int_0^T \|\tilde{d}_i(t) - \tilde{s}_i(t)\|^2 \, dt, \tag{4}$$

where $\tilde{d}_i = e^{i\phi(t)}$ and $\tilde{s}_i = e^{i\phi_s(t,\mathbf{m})}$ are the normalized analytical signals for observed and synthetic data, respectively. ϕ and ϕ_s are the instantaneous phase of observed and synthetic data, respectively. Indices s and r indicate sources and receivers.

To balance the uneven distribution of earthquakes and seismic stations we introduced a geographical weighting to our misfit function, following (Ruan et al., 2019). For each receiver r_i, a weight w_i is calculated according to Equation 5:

$$w_i = \left[\sum_{j=1}^{N_p} e^{-\left(\frac{D_{ij}}{\Delta}\right)^2} \right]^{-1}, \tag{5}$$

where D_{ij} denotes the distance between two stations for all N_p pairs that include the receiver r_i. A reference distance Δ is used so that the condition number of the matrix given by Equation 5 is not too large. In practice, it is determined through a linear search so that its value is around 35% of the maximum (Figure 6b). We used the same scheme to balance the source distribution (Figure 6a).

3.3. Adjoint Simulations

Adjoint simulations were carried out to compute Fréchet derivatives (Tromp et al., 2005) where the result of each simulation per earthquake gives the summation of Fréchet kernels that leads to event kernels (Tape et al., 2007). Similar to forward simulations, topography/bathymetry, the ocean load, gravity, rotation, ellipticity were all included in the adjoint simulations. Attenuation was also taken into account in adjoint simulations using partial storage of the forward wavefield (Komatitsch et al., 2016) to ensure accurate sensitivity kernels. We refer to the Supporting Information S1, for the details of numerical simulations.

3.4. Post-Processing Stage

For each iteration, we computed event kernels for the 112 selected earthquakes, and summed them up to obtain the gradient of the misfit function (Equation 4) for each model parameter and the pseudo-Hessian kernel (Equation 6), which was used as a pre-conditioner. The gradients were multiplied by the source weights computed by Equation 5. During the summation, we masked the area around seismic sources to minimize the imprint of source locations in the computed gradients.

Although we filtered adjoint sources with the same band-pass filter applied to seismograms before running the adjoint simulations, we smoothed the gradients of all the parameters using a Gaussian function in the vertical and horizontal directions (Zhu et al., 2015) to remove remaining short-wavelength signals and further balance the imperfect data coverage (Bozdağ et al., 2016). The crust and the upper mantle, where the wavelengths are shorter and the data coverage is better, require less smoothing than the transition zone and the lower mantle. In the first six iterations, we used a horizontal smoothing radius of $\sigma_h = 150$ km and a vertical smoothing radius of $\sigma_v = 15$ km for the crust and the upper mantle. We increased σ_h and σ_v gradually by depth, reaching 200 and 100 km, respectively, at the bottom of the lower mantle. Smoothing was also gradually decreased as the iterations proceeded, progressively including finer details into the model. In the final iteration, we reduced σ_h to 80 km and σ_v to 5 km for the crust and the upper mantle, and to 120 and 60 km, respectively, at the bottom of the lower mantle.

We then weighted the gradients by the inverse of the pseudo-Hessian kernel to velocity up the convergence rate of the inversion. Ideally, we would use the complete Hessian matrix in the optimization process. However, since
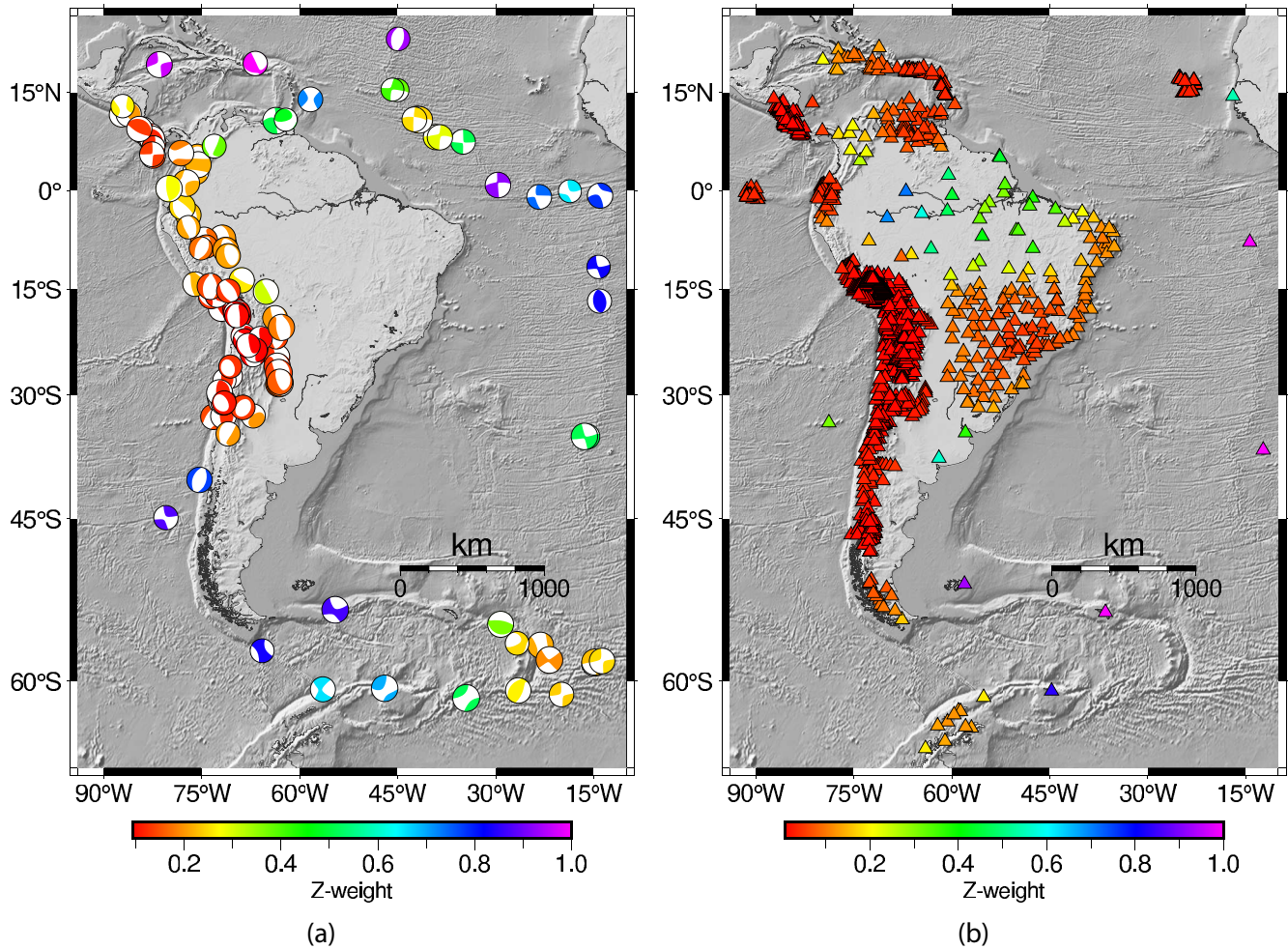
Figure 6. (a) Source weights are applied to each earthquake to balance the geographical distribution by attributing larger weights to more isolated events. (b) Same as (a) but for stations. The receiver weights are applied to the adjoint sources (Section 3.2.3) whereas the source weights are applied to the event kernels (Sections 3.3 and 3.4).

computing it would be prohibitively expensive (Fichtner, 2010), we replaced it by the so-called pseudo-Hessian $P(\boldsymbol{x})$, which approximates the diagonal terms of the Hessian matrix and can be computed using the second temporal derivatives of the forward and adjoint displacement wave fields $s(\boldsymbol{x}, t)$ and $s^\dagger(\boldsymbol{x}, t)$ (Luo et al., 2013):

$$P(\boldsymbol{x}) = \sum_{e=1}^{E} \int_0^T \partial_t^2 \boldsymbol{s}(\boldsymbol{x}, t) . \partial_t^2 \boldsymbol{s}^\dagger(\boldsymbol{x}, T - t)\, dt. \tag{6}$$

The reason for choosing the pseudo-Hessian as a preconditioner is that it resembles data coverage (Luo et al., 2013), which further balances the gradient while suppressing high-amplitude values at source and receiver locations.

3.4.1. Model Update

During the first iteration, we used the preconditioned gradients to update the starting model using the steepest descent method (Debye, 1909). From the second iteration on, we started using the conjugate gradient method (Fletcher & Reeves, 1964) to speed up the convergence. We can keep using the conjugate gradient method as long as we keep the measurement windows fixed or until the gradients lose conjugacy (Fichtner, 2010). Both the steepest descent and the conjugate gradient methods provide the direction d_i in which we should update the model to have the fastest convergence. We then performed a line search (Wolfe, 1969) to determine the step length α for the model update at each iteration. In this study, the line search consists of running forward simulations for a

subset of 41 earthquakes for various values of α, typically ranging from 0% to 3.5% perturbations in the search direction d_i. Using these values (at least four, in our case), we fitted a polynomial and used its minimum as the step size. Then, we updated the model parameters by

$$\ln\left(\frac{m_{i+1}}{m_i}\right) = \alpha\, d_i. \tag{7}$$

4. Assessment of the Model Quality

In this section, we present the assessment of the quality of our model by (a) monitoring the misfit evolution, (b) using cross-correlation travel-time measurements for an independent set of earthquakes not used in the inversion to check the improvement in waveforms by components and period bands, (c) performing Point Spread Function (PSF) tests (Fichtner & Trampert, 2011), and (d) estimating the data coverage density. In addition, we computed mean correlation coefficients by sources and receivers to estimate the improvement in waveform fitting per event and per station.

4.1. Misfit Evolution

We used the misfit evolution as a metric to assess if and how much the phase misfit decreases after each iteration. We observe a large reduction in the misfit after the first iteration, as expected. As the iterations progress, the misfit decreases slower after each iteration and becomes flat, signaling that we are near a minimum of our objective function. Figure 7 summarizes our results after 23 iterations for the total misfit and misfit reduction in each measurement category (different period bands at three components).

As explained in Section 3.2.3, using the phase information only in the misfit function is one way to mitigate the non-linearity of the inverse problem. The multi-scale approach (fitting long-wavelength data first and gradually moving on to shorter wavelengths) is another common method in seismology to mitigate the problem since fewer local minima exist at longer wavelengths (e.g., Bunks et al., 1995; Van der Lee & Nolet, 1997). We used a single period band during the first five iterations, including signals between 50 and 100 s.

We chose 50 s as the minimum period in these first iterations because our starting model S362ANI (Kustowski et al., 2008) was inferred from 35 to 150 s surface waves and long-period (above 50 s) body waves. The maximum period was set to 100 s because that was the upper period band corner we used when removing instrument responses, to avoid amplification of low-frequency noise in the data.

After about 20% reduction in the overall misfit, we recomputed the measurement time windows. Due to higher similarity of observed and synthetic waveforms, more data was selected and windows were enlarged and merged. This inclusion of additional data explains the increase in the misfit from iteration 4 to 5. We carried out two additional iterations (5 and 6) using the new windows. Because the misfit reduction was slowing down, we reduced the lower period of our band from 50 to 40 s at iteration 7. We performed five more iterations with the newly selected measurement windows in which we observed a continuous decrease in misfit.

At iteration 11, we noticed short-wavelength artifacts in the lower mantle, indicating that we needed to smooth the gradients below the transition zone further. We first filtered the lower mantle by using the new smoothing parameters ($\sigma_\text{h} = 200$ km and $\sigma_\text{v} = 100$ km) which were also applied to the new gradients. The filtering process increased the misfit by a negligible amount ($\sim$0.1%), confirming that our measurements have reduced sensitivity to lower-mantle structure.

After three more iterations, the misfit nearly stagnated. At that point, to further reduce the minimum period of measurements, the resolution of our simulations was increased by interpolating the NEX = 128 resolution mesh, where NEX is the number of spectral elements on each side of chunk at the surface (see the Supporting Information S1), to an NEX = 192 (i.e., a 50% increase in the spectral-element density). The higher resolution can accurately simulate the wave propagation down to a minimum period of $\sim$23 s. At this stage we defined a second-period band, ranging from 30 to 60 s. The higher-frequency data had larger misfits than the, already fit, low-frequency data, resulting in the window-selection algorithm selecting more data in the lower-frequency bands. To ensure that each frequency band had equal contribution to the overall misfit, we weighted the adjoint
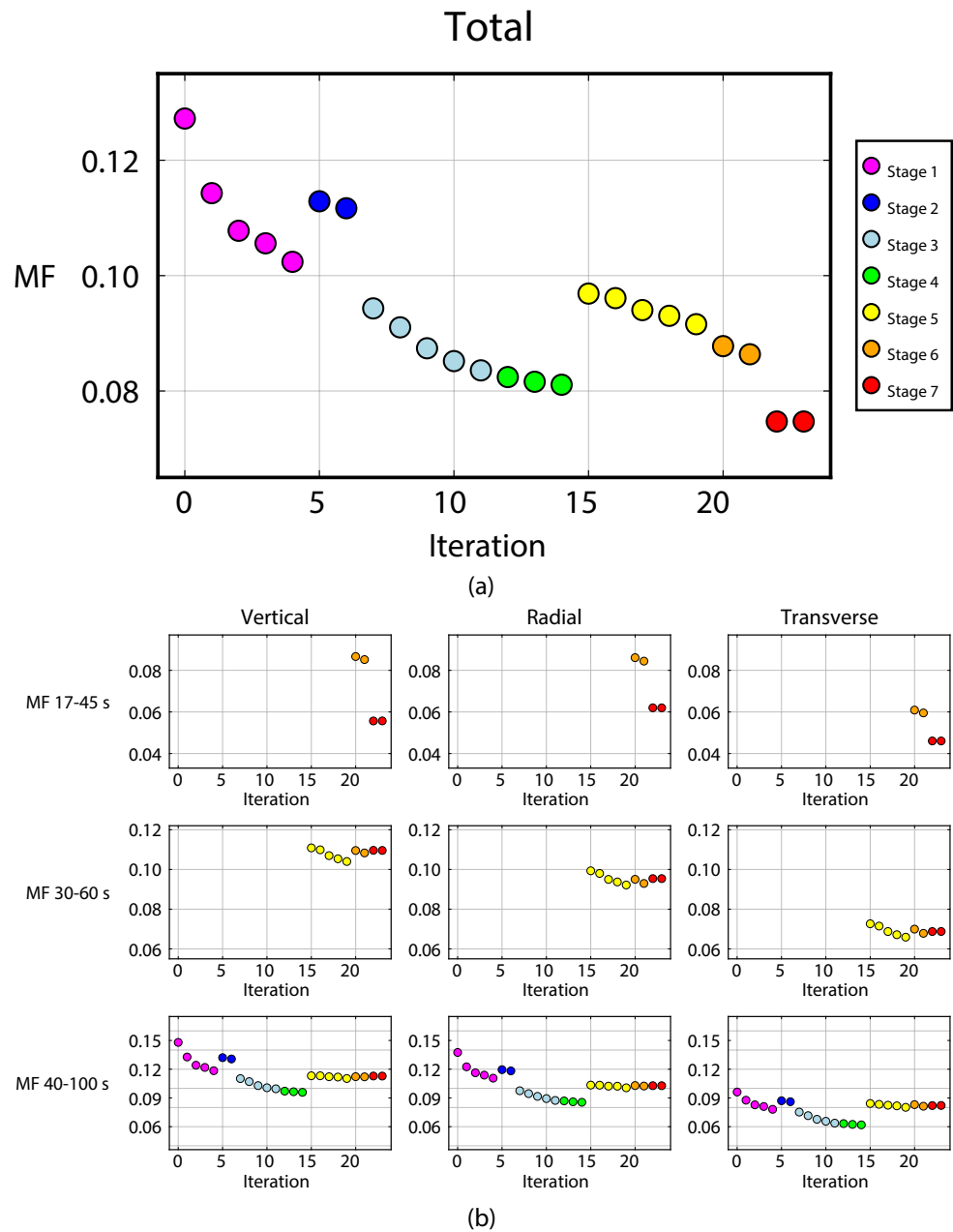
Figure 7. Upper large figure (a): Overall misfit (MF) drop after each iteration. The values in the vertical axes were averaged by the number of measurements which, in our case, is the total number of seismogram components approved for window selection in each category. Different colors denote different time windows. Usually, an increase in MF from one stage to another is caused by larger windows including more data or by the addition of another period band. On the other hand, decreases in MF between stages are a combination of model improvement with reduction of data selected. Lower small figures (b): MF drop for each period band. The MFs are smaller in the transverse component because less data is selected in that component, reducing its contribution to the overall MF. In all cases, the MF is dimensionless.

sources of each band by a constant inversely proportional to the amount of data selected (i.e., the total length of all the combined windows) before summing them.

We kept the windows fixed from iteration 15 to 19, entering another cycle of continuous misfit reduction. At iteration 20, we added a third frequency band, 23–45 s. We recomputed the windows and carried out two additional iterations. Finally, at iteration 22, we interpolated the mesh once more to increase its resolution from NEX = 196 to NEX = 256 (i.e., a 33% increase in the spectral-element density). We decreased the lower period

of measurements from 23 to 17 s. Six seconds of period reduction represents a ~26% increase in frequency. At that period range, such an increase had an important impact on the waveform complexity, causing a considerable reduction in the amount of data selected, observed as a large drop in the misfit from iteration 21 to 22. We recomputed the windows for the last time and carried out two more iterations, but the misfit remained nearly unchanged. Therefore, we ended the inversion at iteration 23.

We compared models M00 and M23 by computing synthetic seismograms down to a period of ~17 s. Here we had two choices, each with their own pros and cons: Either we used the windows computed using the M00 synthetic seismograms and lost the information for a considerable amount of waveforms that were selected only at M23, underestimating the improvement in waveform fitting, or we used the windows computed using the M23 synthetic seismograms and ran into the risk of cycle-skipping on the M00 synthetics, overestimating the overall misfit reduction. The latter was the lesser con in our case because EP measurements tamper phase differences larger than $\frac{\pi}{4}$, limiting the effect of possible outliers on the overall misfit. Using this second approach shows a 50% reduction in misfit.

We should expect a smaller estimate of improvement in waveform fits when using the first approach, given that the windows computed for M00 only include sections of the seismograms that were already reasonably fit since the first iteration. Indeed, by using the first approach, we found an overall reduction of 11% from M00 to M23. Because both estimates have their limitations, we further assessed the improvement in waveform fits using approaches that are more resilient to cycle-skipping, presented in the following sections.

4.2. Cross-Correlation Travel-Time Residuals

The misfit reduction attributes a single value for each period band and component. We measured the overall reduction in the phase residual for all waveforms, but we did not know the behavior of the residuals individually in each segment of seismograms. We measured the misfit reduction in the same data set used in the inversion that minimizes it. A more robust and informative metric would assess waveform fit improvement in an independent data set that was not used in the inversion. To this end, we computed the misfit based on cross-correlation travel-time measurements where we re-selected smaller measurement windows appropriate for cross-correlation measurements using M23. To compute the histograms, we downloaded the waveforms of all the events with M_w = 6–7 from the GCMT catalog in the region of interest, between 14 August 2018, and 3 November 2020 (53 events altogether), a period not used in the inversion. Then, we ran NEX = 256 resolution forward simulations to generate the synthetic seismograms both for the starting model (M00) and for the final model (M23). Figure 8 shows all the residuals grouped by component and period band. The histograms show that, even using an independent set of data, we observed a substantial improvement from M00 to M23 based on cross-correlation travel times. Another advantage of using travel-time histograms is that cycle-skipped measurements with the largest time shifts are easy to identify and separate from the reliable measurements because they appear as secondary and much smaller peaks, outside the $[-T_{min} \leq \Delta T \leq T_{min}]$ interval, where T_{min} is the minimum period in which band. In Figure 8 we only show measurements within their respective $[-T_{min}, T_{min}]$ intervals, mitigating the influence of cycle-skipping in our analysis.

The most obvious improvement after 23 iterations is the narrower histograms for all the nine categories (Figure 8) nicely centered around zero. Our observations based on cross-correlation measurements are also important to show the robustness of EP measurements which, to the best of our knowledge, is used in a 3D adjoint tomography study with real data for the first time.

#### 4.2.1. Correlation by Source and Receiver

Another useful analysis to assess the improvement of the final model over the initial one is comparing the mean correlation coefficient per event and per station for the original data set (the same used in the inversion). However, unlike the previous subsections, this time, we did not use any windows. For each trace that was accepted for measurement (i.e., not rejected by the windows selector), we calculated the correlation coefficient between the observed and synthetic filtered from 40 to 100 s, without excluding any segment of the seismogram and without shifting any of the traces. That coefficient is a measure of the waveform similarity between the two traces.

By computing the mean of the coefficients, we evaluated the overall waveform similarity for each source or receiver. Since we were not subdividing the seismograms into multiple disconnected windows, the correlation
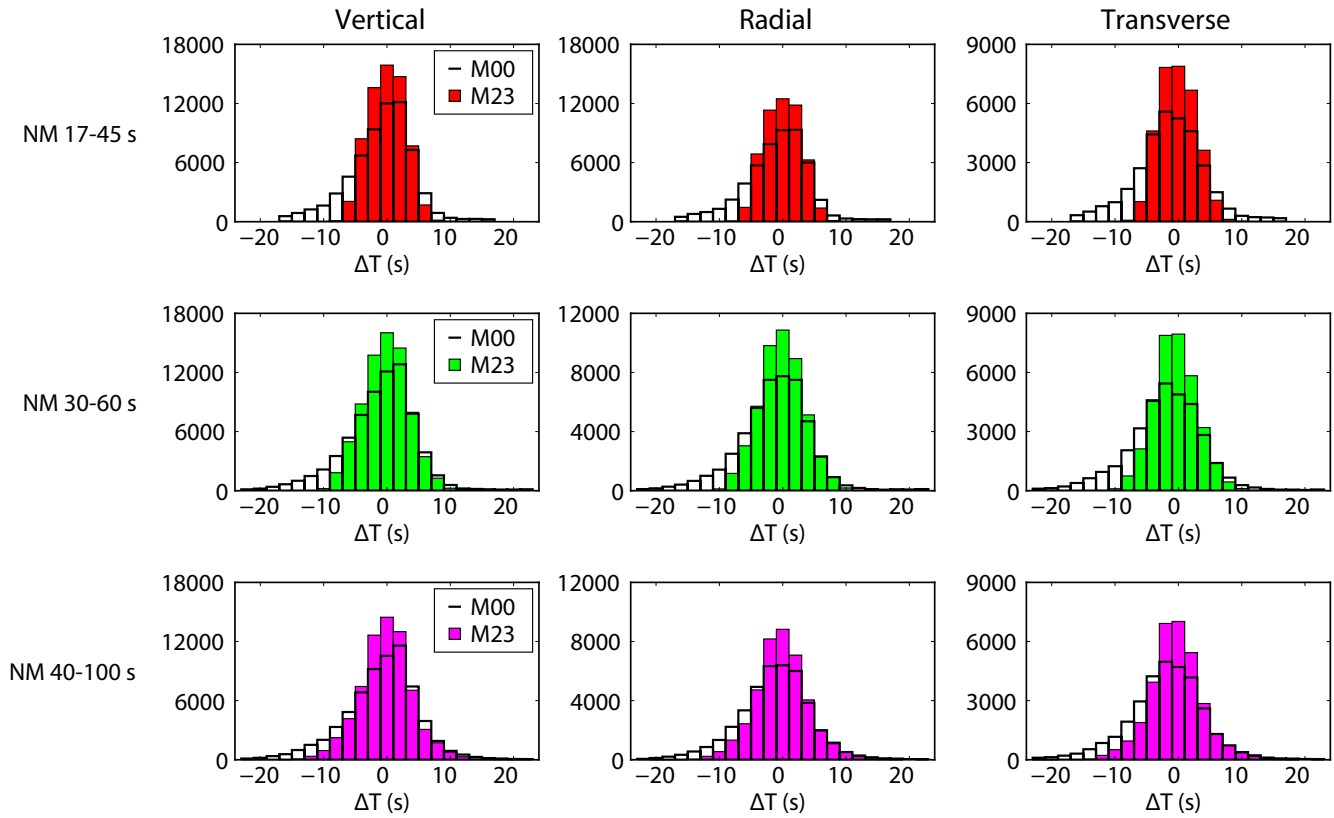
Figure 8. Comparison between the travel-time residuals histograms of M00 (black line) and M23 (colored bars) grouped by component and period band. NM stands for the number of measurements and ΔT represents the time shift.

coefficient is dominated by the largest amplitudes, which are the surface waves. Despite this limitation, this analysis is useful for identifying outliers (events or stations) and for assessing model quality and improvement per region, without being affected by cycle-skipping. Figure 9 shows that for both sources and receivers, there is
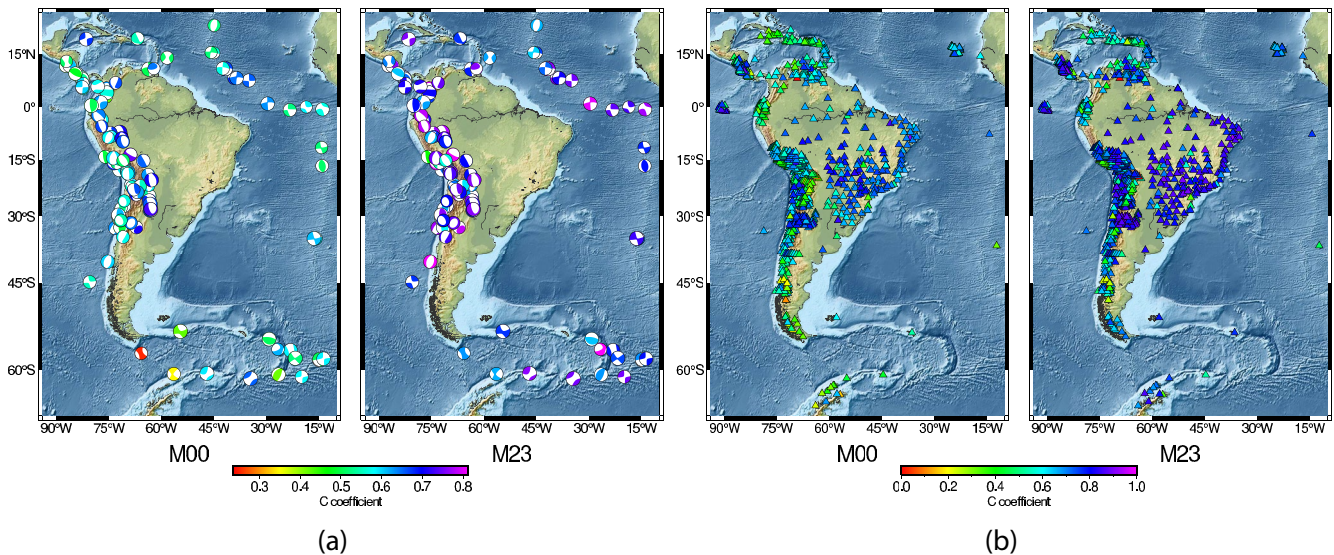
Figure 9. (a) Mean correlation of all the 1,311 stations per event for M00 and M23. The overall correlation coefficients for M00 and M23 are 0.58 and 0.70, respectively. (b) Mean correlation of all the 112 events per station for M00 and M23. The overall correlation coefficient for M00 and M23 are 0.55 and 0.65, respectively.

an improvement in waveform similarity after 23 iterations. For example, as shown in Figure 9b, we notice that the model better explains waveform data in Brazil, the central Andes, and oceanic regions. Less impressive fits are achieved in the southern portion of South America and especially in the Caribbean, both of which are highly tectonically complex regions.

4.3. Resolution Tests

The inversion of synthetic data generated for checkerboard or tectonic-structure models are commonly used in linearized seismic tomography to estimate resolving power (e.g., Celli et al., 2020; Feng et al., 2007; Fukao et al., 1992; Grand, 1987; Inoue et al., 1990; Zelt, 1998). Despite the relevance of those tests, they are infeasible in adjoint tomography, as they cost as much as the actual iterative inversions. Fichtner and Trampert (2011) introduced "Point Spread Functions" (PSF) in adjoint inversions as a way of directly estimating the model resolution at a given spot using a finite-difference approximation to calculate the local action of the Hessian $H \cdot \delta m$ without the need of the actual Hessian H (Equation 8):

$$H \cdot \delta m \approx g(\tilde{m} + \delta m) - g(\tilde{m}), \tag{8}$$

where H represents the Hessian, δm is the localized Gaussian model perturbation with respect to the optimal model $\tilde{m}$, $g(\tilde{m})$ is the gradient at $\tilde{m}$, and $g(\tilde{m} + \delta m)$ is the gradient at $\tilde{m} + \delta m$. The principle underneath the method is that in the vicinity of the optimum, the Hessian describes the convexity of the objective function, providing a direct measurement of the resolution and trade-offs in the misfit caused by δm (Fichtner & Trampert, 2011).

Figure 10 shows point spread functions for four regions we selected based on data coverage and tectonic and geological features: the middle of the Central Brazil Shield (Figures 10a and 10b), the Paranapanema Block (Figures 10c and 10d) at 110 km depth, the Nazca Plate near 15°S (Figures 10e and 10f) at 1,100 km depth, and south Brazil (Figures 10g and 10h) at 2,500 km depth. The two Gaussian perturbations at depths of 110 km have a diameter of 100 km. The perturbation at 1,100 km is 130 km in diameter and the perturbation at 2,500 km is 150 km. All of the four anomalies are spherical. Figure 10 shows that the deeper the perturbation, the more blurred is the recovered result. The amount of blurring is a inverse proxy of resolution. In the Supporting Information, we show four additional resolution tests. Three of them at 150 km depth: in the Andes (Figures S5a and S5b in Supporting Information S1), at 40°S, in the Borborema Province (NE Brazil; Figures S5c and S5d in Supporting Information S1), and in Venezuela (Figures S5e and S5f in Supporting Information S1). For these last three, we used 100 km Gaussian perturbations. The last resolution test is inside the Nazca Slab at 500 km depth (Figures S5g and S5h in Supporting Information S1).

By comparing the white contours (showing half the peak amplitude) with the green 500 km diameter reference circumferences (Figure 10), the vertical resolution of the model at 110 km depth is estimated to be around 150 km. The resolution decreases to ~390 km at 1,100 km depth, and to around 550 km at 2,500 km depth. The horizontal resolution corresponding to these same depths are, respectively: 500–850, 550–660, and 670–1,700 km. The three additional resolution tests at 150 km depth (Figure S5 in Supporting Information S1) indicate a vertical resolution ranging between 200 and 250 km. In the Nazca Slab, at 500 km depth, it decreases to 350–380 km (Figure S5 in Supporting Information S1). The corresponding horizontal resolutions at 150 and 500 km depth are, respectively: 500–1,100 and 360–380 km.

4.4. Coverage Density Analysis

PSF tests provide an estimate of the model resolution at select locations, but they are computationally expensive and not practical for assessing resolution at larger scales. A region-wide estimate of data coverage can complement the resolution analysis of the PSF tests. The pseudo-Hessian can resemble the data coverage by taking into account the amplitude effects associated with geometrical spreading of both the forward and adjoint wavefields (Luo et al., 2013). For phase measurements, Luo et al. (2013) suggest creating a finite-frequency version of the ray density (hitcount) maps from classical methods by summing cross-correlation based finite-frequency (banana-doughnut) kernels for all measurements after setting all travel-time delays ΔT_i equal to one.
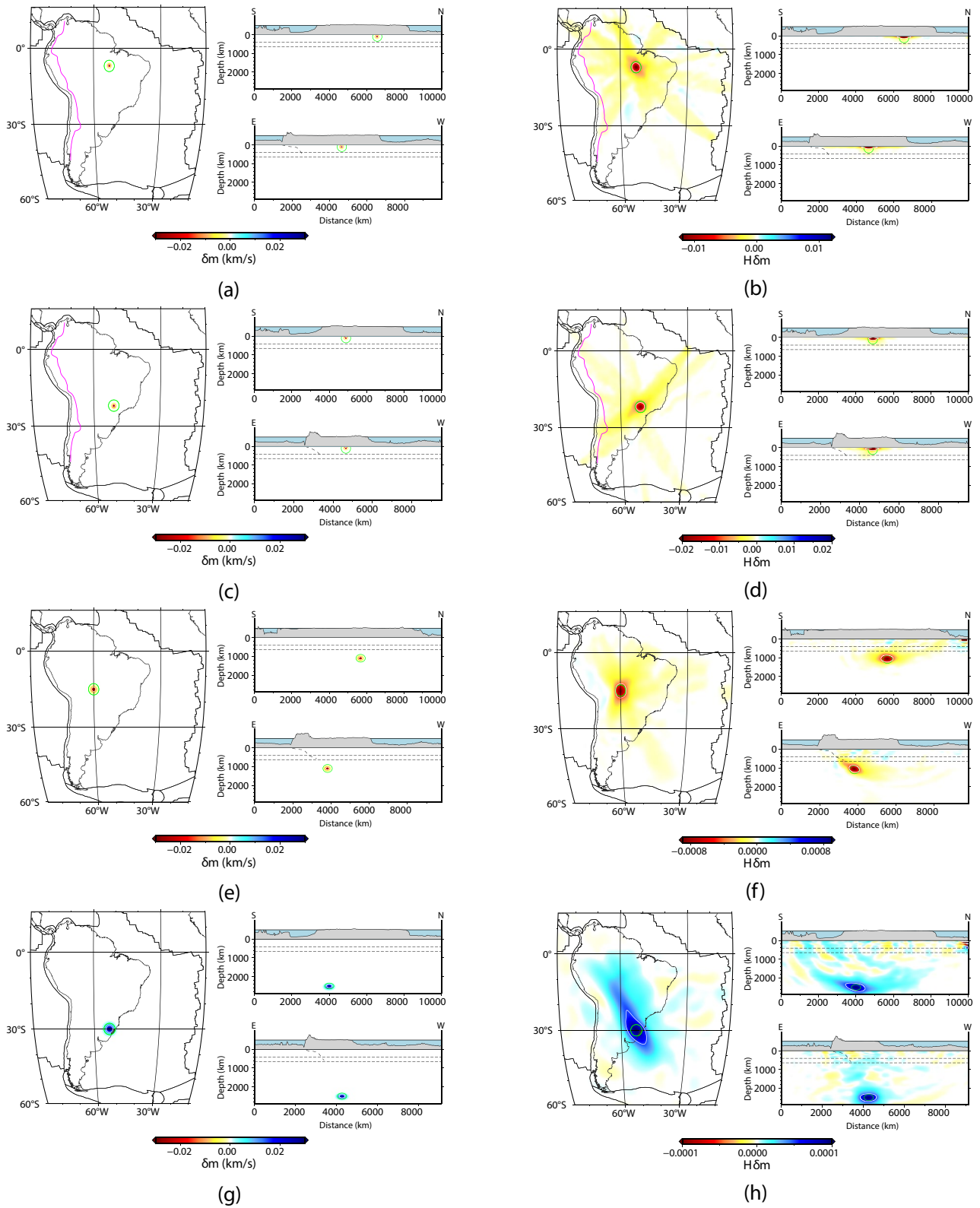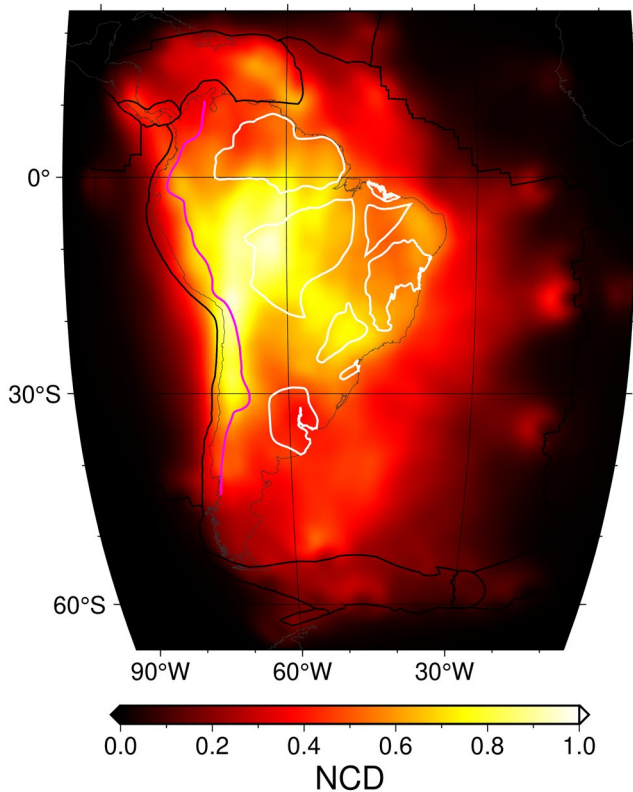
Figure 10.

Figure 11. Normalized coverage density (NCD) at 110 km depth. The white contours show the cratons (Figure 1) and the magenta line shows the top contour of the Nazca Slab according to Slab2. There is next to no coverage outside the region in which the sources and receivers lie. As expected, the highest coverage occurs in regions with denser seismic network arrays (e.g., northern Chile and southeastern Brazil) or where ray paths cross more often (e.g., Amazon).

Rather than using the actual kernels computed via the adjoint method, for performance reasons, we replaced them with approximate kernels, computed using a combination of Gaussian functions (Equations S1 and S2 in Supporting Information S1) around the ray paths of the phases used in our inversion. Ray tracing was carried out using the ObsPy (Beyreuther et al., 2010) implementation of TauP (Buland & Chapman, 1983; Crotwell et al., 1999) assuming model AK135f_no_mud (Kennett et al., 1995; Komatitsch & Tromp, 2002a, 2002b; Morelli & Dziewonski, 1993).

To approximate body-wave kernels, we recreated a *hollow-banana*-like structure in which the first Fresnel zone was larger and negative, and the second one is smaller and positive (Marquering et al., 1999; Woodward, 1992). For surface waves, we considered the non-zero sensitivity at the ray path (Dahlen & Zhou, 2006; Zhou et al., 2004). We also took into account the sensitivity variations with depth by mimicking the sensitivity profiles in Takeuchi and Saito (1972), Yoshizawa and Kennett (2005), Lebedev and Van der Hilst (2008), Liu et al. (2016), Zhang and Yao (2017), and Qiao et al. (2018). Then, we summed the absolute values of all the approximate kernels and normalized the final result by the maximum coverage of all depths (Figure S8 in Supporting Information S1). Figure 11 shows the resulting map at 110 km depth. We explained the method in detail in the Supporting Information (Figure S6 in Supporting Information S1). For depths down to 900 km, the coverage is similar to that shown in Figure 11, with a maximum achieved at 500 km. The coverage decreases below 900 km to a minimum at 1,500 km (Figure S8 in Supporting Information S1).
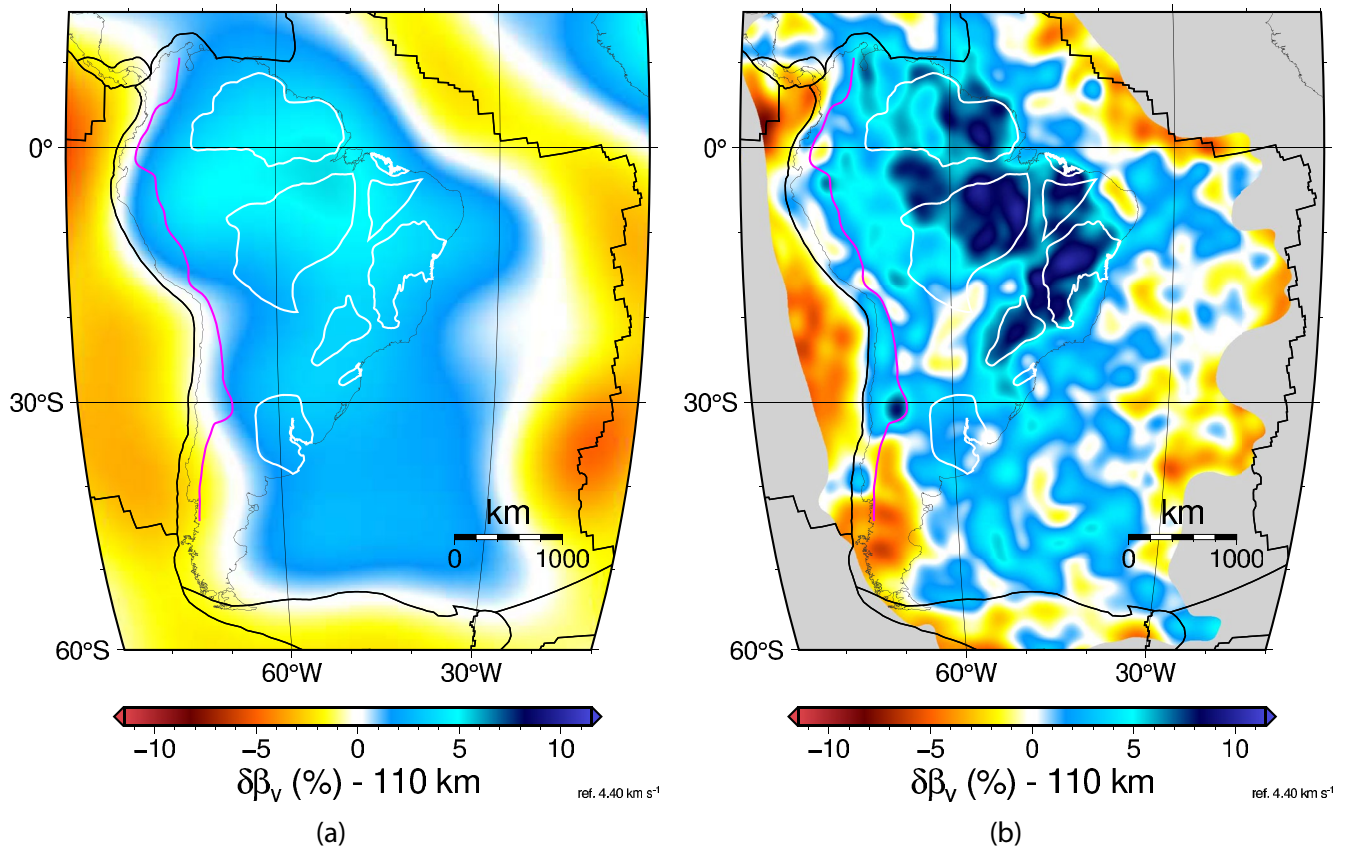
5. Results

Here, we focus our interpretation on the β_v perturbations of SAAM23 because (a) *S* waves are more sensitive to the presence of fluids and partial melting in the Earth's interior than *P* waves, conveying more information despite having a lower-frequency content and (b) the inversion of vertically polarized waves includes more data because vertical component seismograms are generally less noisy than the horizontal components. Nevertheless, we present SAAM23's other parameters in the Supporting Information (Figures S9–S13 in Supporting Information S1) as well as the average reference model (Figure S14 in Supporting Information S1). Although the model for β_v correlates better with geological and geophysical features, β_h, α_v, and α_h show similar trends of high velocities beneath cratonic blocks, as well as image the Nazca Slab down to about 900 km depth (Figures S9–S13 in Supporting Information S1).

5.1. Overview

Figure 12 shows M00 (S362ANI + CRUST1.0), our starting model, and the final model M23 (SAAM23). In SAAM23, we identify structures such as a low-velocity anomaly beneath the South Sandwich Islands subduction zone, and beneath the spreading center connecting the Cocos and the Nazca plates to the north of the Galapagos Islands. In the South Atlantic region, the contour of the Argentine Basin is imaged as a high-velocity ring around the sedimentary basin. At 30°S in the Andes, a distinct high-velocity anomaly shows the shallow-dipping Nazca Plate (Pampean Flat Slab). Strong high-velocity anomalies beneath the Paranapanema and the Parnaíba blocks

Figure 10. PSF resolution analysis for four points in the model. The left column (a, c, e, and g) shows the perturbations δm, and the right column (b, d, f, and h) shows the corresponding action of the Hessian $H \cdot \delta m$. The widths of the Gaussian perturbations were adjusted roughly to match the minimum wavelength expected to be resolved at each depth, according to the velocities and the minimum resolved periods, ranging from 100 to 150 km. The perturbations are 0.03 in magnitude, positive at locations with negative velocity anomalies, and negative in the opposite case. In the recovered plots, the white contours show the values that correspond to half of the maximum, allowing an estimate of the resolution by comparison with the green reference circles, which are all 500 km in diameter.

Figure 12. (a) β_v anomalies at 110 km depth for the starting model (M00). The white contours show the cratons (Figure 1) and the magenta line shows the top contour of the Nazca Slab according to Slab2. (b) Same as (a), but now showing the result after 23 iterations (M23). The regions in which the coverage density was below 10% of the maximum were masked to light gray. The color palette was designed to highlight the cratonic nuclei. All % anomalies in this and following figures refer to the average velocity of the SAMM23 model shown in Figure S14 in Supporting Information S1.

(PB) and the SFC denote the thicker lithosphere. Similar to previous tomographic studies, a high-velocity lithospheric mantle is not imaged beneath the Rio de La Plata Craton. The Borborema Province, northeast Brazil, appears as a strong low-velocity anomaly. Finally, high-velocity anomalies are imaged beneath the cratonic nuclei in Central Brazil and the Guyana shields of the AC. These anomalies weaken to the southwest, toward the younger lithosphere of the Rondonian-San Ignacio and Sunsás-Aguapeí geochronological provinces.

5.2. The Subducting Nazca Slab

The subducting Nazca lithospheric slab is imaged as a narrow high-velocity belt parallel to the Andean margin (especially between depths of 300 and 1,000 km, as seen in Figure S8 in Supporting Information S1). Here we discuss the main features of the subducted Nazca Plate as imaged in SAAM23 and compare them with previous models (e.g.,Celli et al., 2020; Gao et al., 2021; Lei et al., 2020; Li et al., 2008; Montelli et al., 2006; Obayashi et al., 2013; Portner et al., 2020; Rodríguez et al., 2021; Simmons et al., 2012).

5.2.1. Slab Continuity Near Peru

The continuation of the flat slab segment beneath Peru into the deeper upper mantle has not been consistently imaged. Some global models, such as UU-P07 (Amaru, 2007), MITP08 (Li et al., 2008), and Detox-P1 (Hosseini et al., 2020) show a gap in the high-velocity belt in the depth range 300–500 km (Figure 13). The South American regional model of Celli et al. (2020) images the flat slab beneath Peru but does not show it continuing downdip, between depths of 250–400 km (Figures S18 and S19 in Supporting Information S1). Seismicity in the Benioff zone beneath Peru is not continuous: earthquakes occur down to ~250 km, and then near 660 km, with no activity in between. This could lead to an interpretation of the absence of the Nazca Slab in that region. However, other
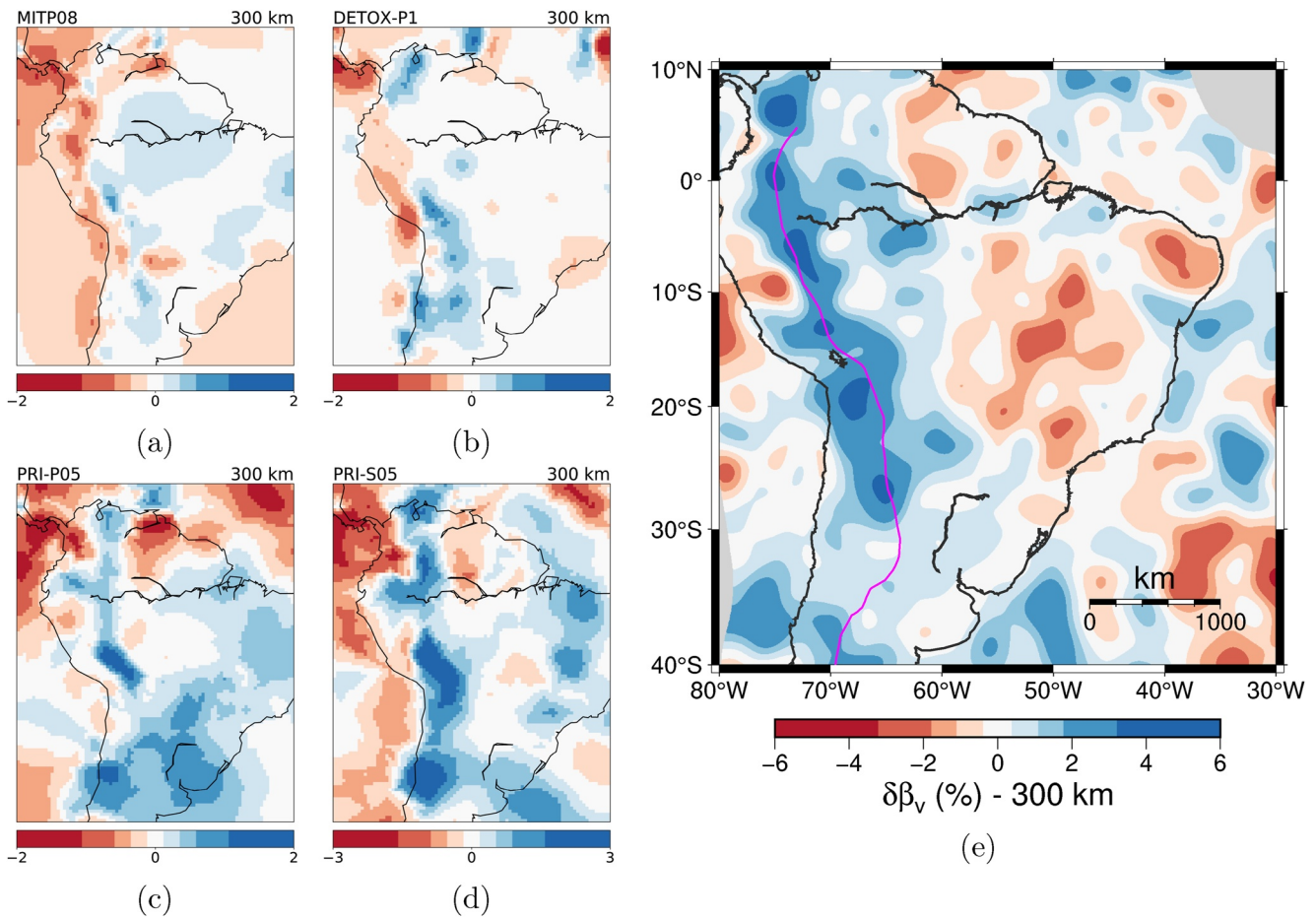
Figure 13. The Nazca Slab east of Peru (from about 6°S to 3°N) is not imaged in some models such as MITP08 (Li et al., 2008; Figure 13a) and DETOX-P1 (Hosseini et al., 2020; Figure 13b), but was seen in the models PRI-P05 (Figure 13c), and S05 (Figure 13d; Montelli et al., 2006). Our model SAAM23 (Figure 13e) shows high-velocity anomalies confirming a continuity of the Nazca Slab in that region. The maps of the four previous models were plotted with the Oxford SubMachine tool (Hosseini et al., 2018).

global models, such as PRI-P05 (Montelli et al., 2006), Detox-P3, and G3Dv3 (Simmons et al., 2012) show a continuation of the high-velocity slab in that region, albeit with lower amplitude. GLAD-M25 (Lei et al., 2020) also shows high-velocity anomalies in the 300–400 km depth range (Figures S20 and S21 in Supporting Information S1). The regional model SAM5-P-2019 of Portner et al. (2020) shows alternating high and low velocities in that region. Moreover, James and Snoke (1990) inferred a continuous slab based on an observed seismic phase that most likely reflected off of the slab surface in the purported gap.

SAAM23 confirms the previous findings of GLAD-M25 (Lei et al., 2020) showing a continuous slab in that region and no evidence for a slab gap or absence (Figure 13). However, the slab's high-velocity anomaly downdip from the Peruvian flat segment has lower amplitudes at depths around 400 km, compared to the Bolivian and Argentinian slab anomalies to the south and the North Andean ones to the north.

This part of the slab with reduced anomaly amplitudes may be related to an anomalous part of the Nazca Plate that subducted during the Neogene, such as an oceanic plateau or island. This diminished anomaly amplitude, together with a limited station coverage in that region, might explain the absence of the slab image in some tomographic models. Such an anomaly might also have been a contributing factor to the small dip angle of the shallow Peruvian slab, and if so, the anomaly's current location would suggest that the Nazca Slab beneath Peru is beginning to steepen.
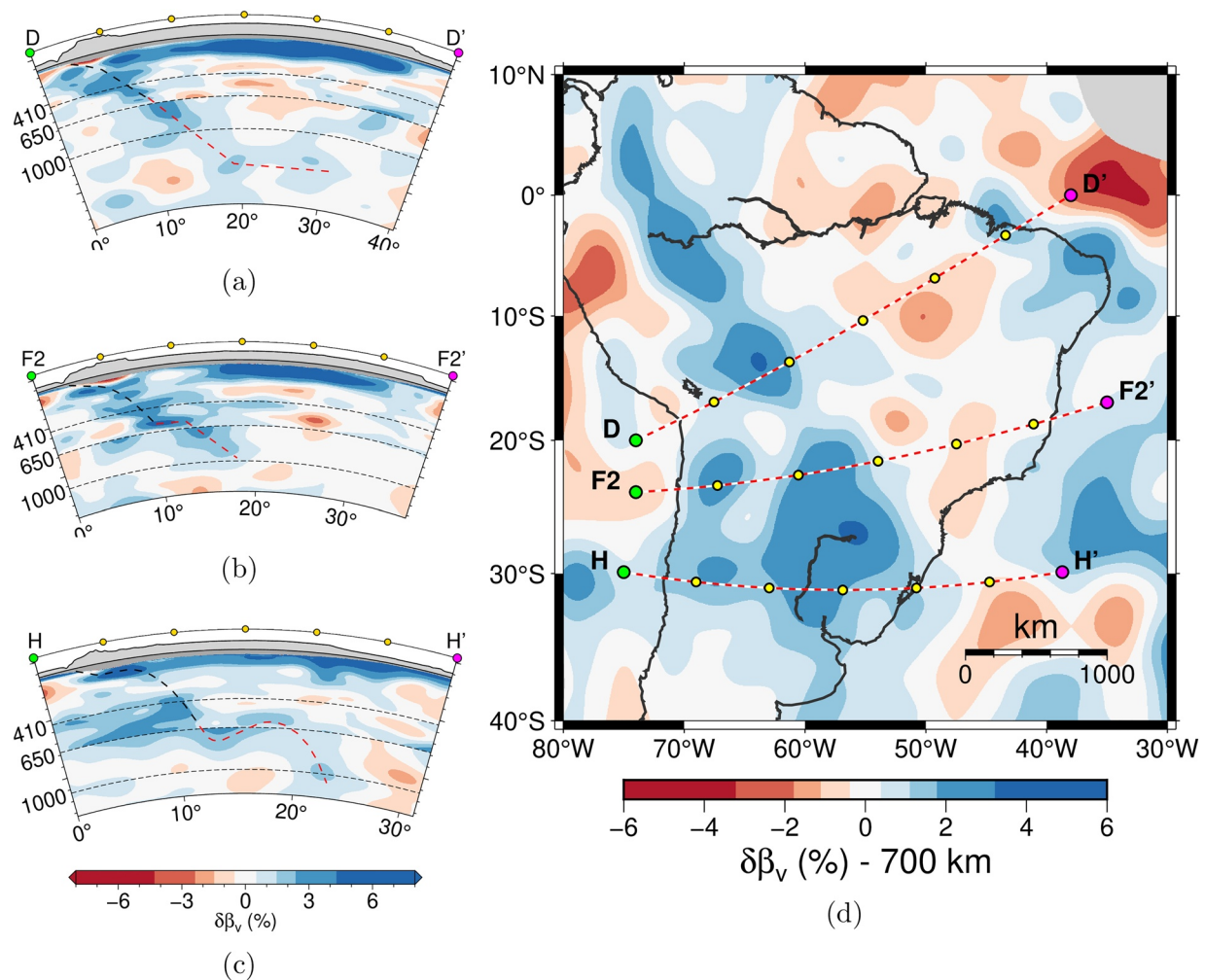
Figure 14. Changes in the Nazca Slab geometry from north to south. North of ~20°S the slab plunges across the transition zone directly into the lower mantle, as seen in profile D. South of ~20°S the slab flattens near the bottom of the transition zone for a while before plunging into the lower mantle (profiles F2 and H). The black dashed line is the Slab2 model after the Benioff zone; the red dashed line is a suggested continuation of the slab further down.

5.2.2. The Nazca Slab in the Lower Mantle

North of about 20°S, several tomographic models image the Nazca Slab crossing the transition zone and continuing into the lower mantle, such as the global models LLNL-3Dv3 (Simmons et al., 2012), GAP-4 (Obayashi et al., 2013), SPani-P,S (Tesoniero et al., 2015), DETOX-P1 (Hosseini et al., 2020), as well as the regional models SAM-P-2019 and SAM-S-2020 (Portner et al., 2020; Rodríguez et al., 2021), as shown in Figure 14. Our model, SAAM23, confirms this slab behavior, including its apparent flattening below a depth of 1,000 km (Figure 14, profile D).

However, near about 20°S, some tomographic models show the Nazca Slab to flatten at the bottom of the transition zone, just above the 660 km discontinuity, such as LLNL-G3Dv3 (Simmons et al., 2012) and GAP-P4, whereas models SAM-P2019 (Portner et al., 2020) and DETOX-P1 (Hosseini et al., 2020) show a straighter continuation of the slab into the lower mantle. The waveform modeling inversion of Celli et al. (2020) appears to be in agreement with the former models, suggesting a slab crossing the transition zone beneath the Amazon and Central Brazil and a trend of stagnation near 660 km depth further south (see Figure S18 in Supporting Information S1). SAAM23 (Figure 14, profile F2) shows intermediate behavior: the slab seems to flatten for a short distance at the bottom of the transition zone, then resumes a straighter trajectory into the lower mantle further east.
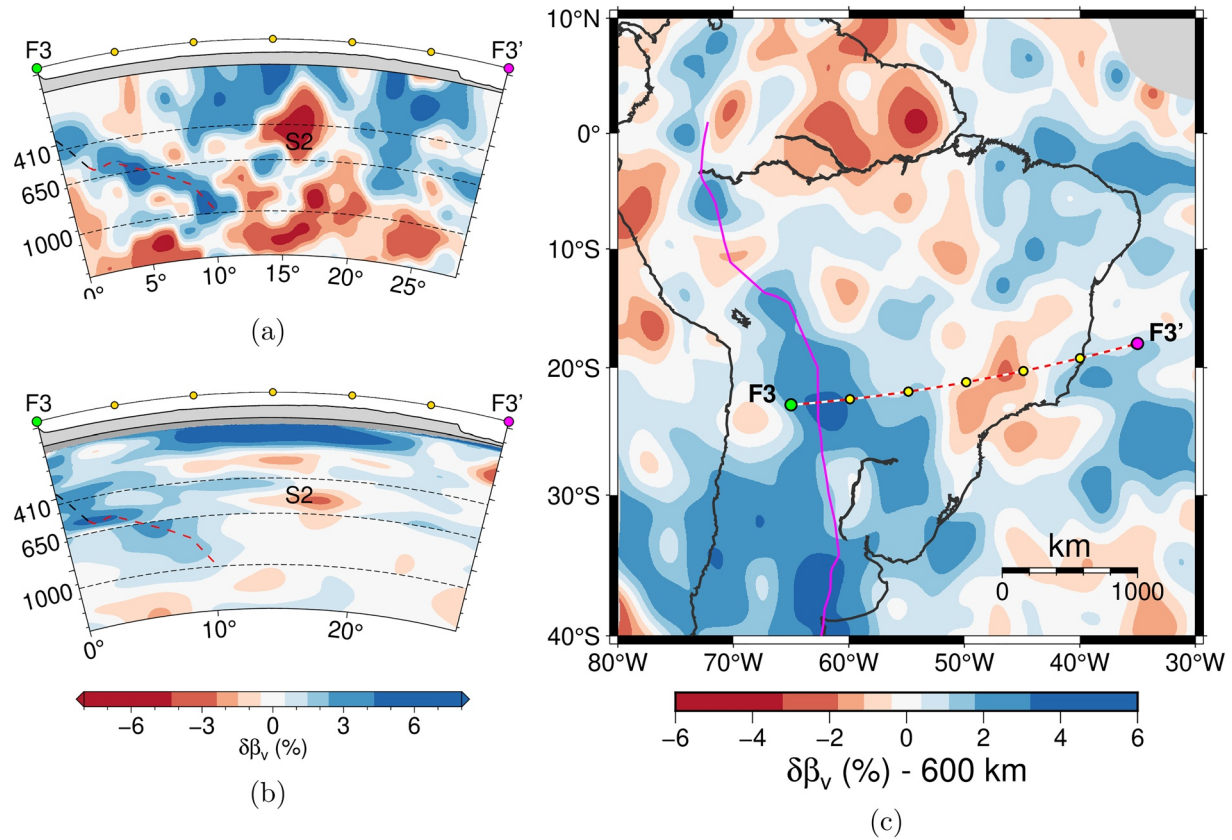
Figure 15. The low-velocity "Paraná Plume" imaged by (a) the *S*-wave teleseismic tomography of Rodríguez et al. (2021) and (b) the SAAM23 model. (c) maps of β_v anomalies at 600 km depth with the profile location. The two dashed lines in the vertical sections are the 410 and 650 km discontinuities.

Further south, around 30°S and in the transition zone, the Nazca Slab has been imaged as a relatively flat high-velocity anomaly along and near the 650 km discontinuity, suggesting either a diminished slab pull (stagnation) just above or just below the transition zone or reflects a change in convergence rate or westwards trench migration (Rodríguez et al., 2021). Our model (Figure 14, profile H) shows this deep, flat slab segment to be around 1,000 km long, and it seems to be descending into the lower mantle in two separate parts. A similar image was obtained by Rodríguez et al. (2021) (their Figure 7d, our Figure 14c). Rodríguez et al. (2021) interpret this behavior as the result of spatio-temporal changes in the rate of westwards trench migration rather than as a change in slab pull with depth. If heterogeneous slab pull is a factor, it is possible that the cause lies in the same lithospheric anomalies that might have caused shallow subduction at small dip angles in the past.

Moving further southwards, around 46°S, a region of very low shear wave velocity that spans most of the Patagonian Domain in SAAM23 (Figure 12), previously observed by Feng et al. (2007) and Celli et al. (2020), correlates with the slab window proposed by Russo, Gallego, et al. (2010) and Russo, VanDecar, et al. (2010) in front of the Nazca-Antarctica-South America triple junction.

5.2.3. The Paraná Plume

A vertical "cylindrical" low-velocity anomaly beneath the Paraná Basin, first detected by VanDecar et al. (1995), was confirmed and extended down to ∼800 km by Schimmel et al. (2003) and Rocha et al. (2011). The initial interpretation of the anomaly as due to higher temperatures was challenged by Liu et al. (2003) and Bianchi et al. (2021) who did not observe any depth changes of the 410 and 650-km discontinuities, based on receiver functions, that could be attributed to a thermal anomaly. Portner et al. (2020) and Rodríguez et al. (2021) showed a low-velocity anomaly in the 150–1,200 km depth range beneath the Paraná Basin, which appears to connect to the Nazca Slab in the top of the lower mantle and transition zone (Figure 15a). SAAM23 also shows low velocities from 250 km down to the bottom of the transition zone, consistent with previous models (Figure 15b). Rodríguez et al. (2021) suggested that this low-velocity anomaly may represent a current mantle upwelling induced by the
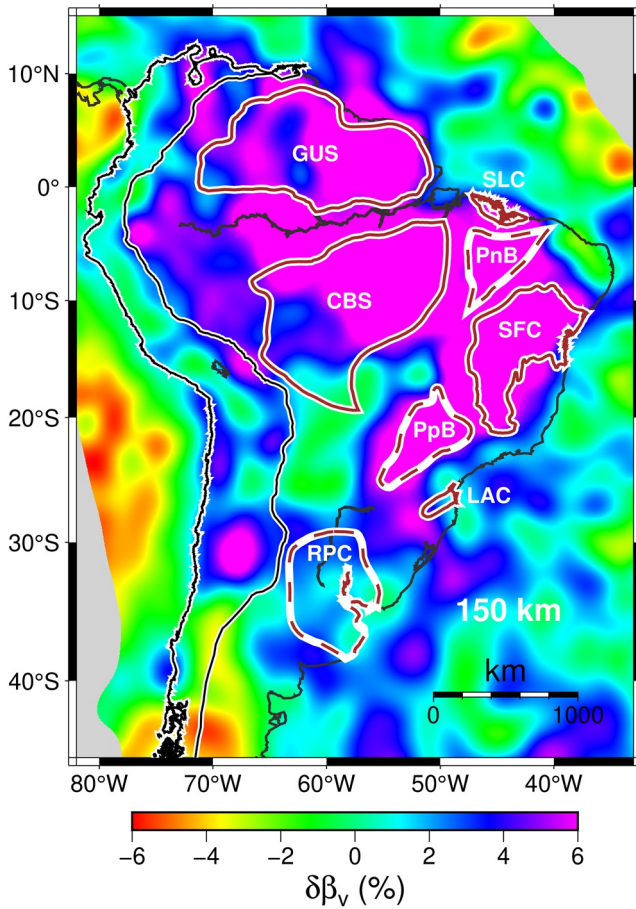
Figure 16. Lithospheric β_v anomaly at 150 km depth and the cratonic units in South America. Exposed cratons: GUS, Guyana Shield; CBS, Central Brazil Shield (part of the AC); SFC, São Francisco Craton; SLC, São Luís Craton; LAC, Luis Alves Craton. Covered cratonic blocks: PnB, Parnaíba Block; PpB, Paranapanema Block; RPC, Río de la Plata Craton. The black solid line delimits the Andean Belt according to CPRM.

continued motion of the leading edge of the Nazca Slab or by the accumulation of hydrous minerals from a second phase of deep dehydration in the slab, as hypothesized by Van der Lee et al. (2008).

5.3. The Lithosphere of the Stable Continental Interior

High velocities in the subcontinental lithosphere (SCL) are imaged beneath most cratons down to about 200 km (Figures S9–S12 in Supporting Information S1), especially for the AC and SFC (Figure 16). Higher velocities are observed for the eastern half of the AC, consistent with older radiometric ages (e.g., Santos et al., 2000; Tassinari & Macambira, 1999; Vasquez et al., 2008). High velocities of the SFC lithosphere are also observed to the west of the SFC's surface limit, similar to the surface wave tomography of Feng et al. (2007) and the teleseismic P-wave tomography of Schimmel et al. (2003) and Rocha et al. (2011). This westward extension of the SFC at depth, is consistent with the assumed larger Neoproterozoic São Francisco paleocontinent (Rocha, Azevedo, et al., 2019).

Smaller cratonic fragments such as São Luís, near the equatorial coast, and Luís Alves, near the southeastern coast, are too small to be resolved by our tomographic model. The anomalies related to the São Luís Craton may be overlapping with those of the PnB. The Luís Alves Craton is located in a region that experienced extensional deformation during Atlantic rifting and impact from an associated plume, and may no longer have a deep lithospheric root. However, Figure 16 suggests a possible continuation of the Luís Alves Craton westwards beneath the Paraná Basin, as also inferred from teleseismic P-wave tomography (Affonso et al., 2021).

Two large intracratonic basins (Parnaíba in the north and Paraná in the SE) are thought to overly old cratonic blocks, inferred from radiometric dates of samples drilled from the basement (Cordani et al., 2009), as well as from models of geological evolution (de Almeida et al., 2000; de Brito Neves & Fuck, 2014). These covered cratonic nuclei, named Parnaíba and Paranapanema blocks, have been tentatively delineated by geophysical mapping (e.g., Affonso et al., 2021; Mantovani et al., 2005). SAAM23 (Figure 16) clearly shows high SCL velocities in the two blocks.

The Paranaíba Block is seen as an independent cratonic nucleus, its lithosphere separated from that of the AC and the SFC. This result is in agreement with Celli et al. (2020), whose SA2019 model also shows PnB as an independent body.

The Paranapanema lithosphere is also separated from the surrounding fold belts (Figures 12b and 16) and reasonably consistent with the gravity-inferred limits of Mantovani et al. (2005). These results indicate that any rifting episode during the evolution of the Paraná Basin was not strong enough to affect the thick lithosphere on a regional scale.

The Rio de La Plata Craton (RPC) is buried beneath sedimentary rocks of the Paraná and Chaco basins and different boundaries have been proposed (e.g., Oyhantçabal et al., 2011; Rapela et al., 2011). However, none of the selected tomographic models showed high SCL velocities for this cratonic area, despite the use of different tomographic techniques (Affonso et al., 2021; Feng et al., 2007; Rocha, Azevedo, et al., 2019; Rosa et al., 2016). SAAM23 does not show high velocities below the RPC either (Figures 12b and 16).

5.3.1. The Lithosphere-Asthenosphere Boundary (LAB)

The depth extent of high SCL velocities is commonly used as a proxy for lithospheric thickness. However, as lithospheric anomalies decrease with depth, reference model velocities typically increase with depth and different
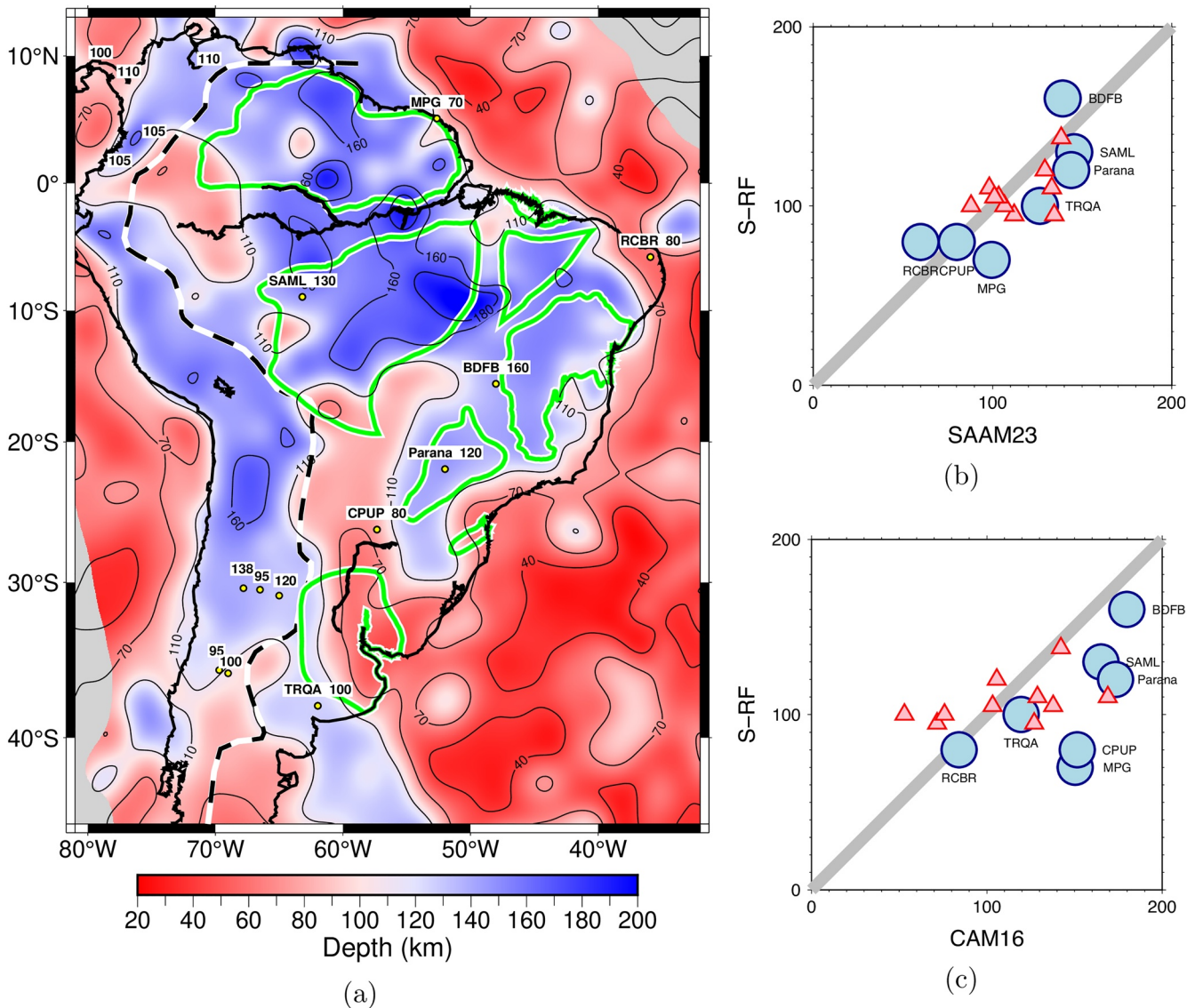
Figure 17. The seismic Lithosphere-Asthenosphere Boundary (LAB) based on the largest negative gradient of the β_v vertical profiles. (a) LAB contours; labeled numbers are LAB depths from *S*-wave receiver functions at seismic stations identified by yellow dots (Heit, Sodoudi, et al., 2007); unlabeled numbers are LAB depths from Andean stations (yellow circles) or regional averages (Blanco et al., 2017; Heit, Sodoudi, et al., 2007). Green lines delimit the cratons and cratonic blocks. The black dashed line is the western limit of the stable continental region (SCR), as defined by Johnston et al. (1994). (b) Comparison of the LAB depth from SAAM23 with those of S-RF: labeled blue circles are SCR stations (Heit, Sodoudi, et al., 2007) and triangles are Andean stations (Blanco et al., 2017; Heit et al., 2008). (c) Comparison of the S-RF LAB with the mechanical LAB depths from the CAM16 model (Priestley et al., 2018), based on geochemical and geotherm criteria, which give about 40 km deeper LAB than our seismic estimates, especially for SCR regions.

tomographic methods experience vertical smearing or decreasing resolution with depth, suggesting an approach that takes this into account.

Our waveform fitting method incorporates both body and surface wave measurements, weakening the trade-off between lithospheric velocity anomaly amplitude and lithospheric thickness. Therefore, we here infer the bottom of the SCL, that is, the LAB, by measuring the depth to the largest negative velocity gradient in each vertical velocity profiles below the Moho (Van der Lee, 2002). For each (1° × 1°) area in our study region we measured the depth to the most negative gradient while applying a Gaussian smoothing filter with 100 km half-width to remove short-wavelength oscillations in the tomography model. Figure 17a shows the LAB map, which has good agreement with the values obtained from *S*-wave receiver function analysis (Figure 17b). We used the LAB depth estimates from the stable continental region (Heit, Sodoudi, et al., 2007), from sub-Andean stations (Heit

et al., 2008), and from regional station averages in Colombia (Blanco et al., 2017). The mean difference between our tomographic LAB and those from *S*-wave receiver functions is about 7 km.

Using the global surface-wave tomography model CAM16, Priestley et al. (2018) estimated the LAB depth using petrological models of the upper mantle and β_v-derived temperature profile to identify the base of the lithosphere as the transition from the conducting to advecting geotherm. This LAB definition gives values about 40 km deeper in the stable continental region than those of the *S*-wave receiver functions (Figure 17c). In the Andes, there seems to be a better agreement of the LAB mechanical definition with those of the S-RF, on average, but the scatter is larger.

In the stable continental region (east of the dashed line in Figure 17a) the thickest lithosphere is found in the AC. A N-S belt of thin lithosphere (near 70 km) is seen from RPC, through the Chaco Basin, and reaching the Pantanal Basin. The northeastern corner of Brazil (Borborema fold province) also has a very thin lithosphere, consistent with the generally SCL low velocities observed by teleseismic *P*-wave tomography north of 7.5°S (Simões Neto et al., 2019) interpreted as due to lateral mantle flow and intraplate volcanism. We observe a thinner lithosphere in the Patagonian Platform, which can be explained by its younger thermal history. The regions of thin lithosphere (less than 100 km) in Figure 17 are also consistent with the higher temperatures (larger than 1,200°C) found by the modeling of Finger et al. (2021).

5.3.2. Lithospheric Thickness and Geochronological Provinces in the AC

The AC evolution is comprised of an Archean proto-craton and a series of accreted terranes, each named as a geochronological province. Different models for the boundaries of these provinces have been proposed. Based on increasing availability of radiometric dates, the model of Tassinari and Macambira (1999) and Tassinari and Macambira (2004) has evolved through Cordani et al. (2016), Teixeira et al. (2019), Macambira et al. (2020), and Johansson et al. (2021). The most up-to-date boundaries, which we call "Model-1," are proposed in Figure 18a. Another set of models for the limits of geochronological provinces, which we call "Model-2," has been proposed by Santos et al. (2000) and Santos (2003). Latter, this model was updated by Vasquez et al. (2008), as shown in Figure 18b. Costa et al. (2020) used this Model-2 to interpret the results of their teleseismic *P*-wave tomography.

Initially, we compared the average *S*-wave anomaly of each province, at 175 km depth (as a proxy for lithospheric thickness), with its age range, to test if older provinces tend to have thicker (colder) lithosphere. Despite *S*-wave velocity heterogeneity within each province, a correlation was found between the average amplitude of the high S-velocities within a province and its geological age, for both geochronological models (Figures 19a and 19c). This trend of increasing velocity anomalies with age is also seen in model SA2019 (Celli et al., 2020).

We also used the direct LAB depth (Figure 17a), instead of β_v anomaly, and a similar conclusion was found: older provinces tend to have thicker lithosphere in the AC, on average (Figures 19b and 19d). Our seismic tomography model cannot indicate the preferred geochronological model, as both show similarly good correlation between age range and lithospheric average depth. The trend of thicker lithosphere with age observed in the Amazon craton is similar to the thermal model developed by Artemieva and Mooney (2001), although our seismic depths are shallower than their thermal estimates.

Lithospheric blocks cool very little after the first ∼500 Ma years. Between 1 and 2.8 Ga, the expected decrease in temperature is only ∼50°C (Porter et al., 2019). For 175 km depth, a difference of 50°C should correspond to 0.4%–1.1% decrease in *S*-wave velocity (Goes et al., 2000). Therefore, the temperature difference due to cooling alone cannot explain the difference of $\delta\beta_v$ of 4% (Figure 19) between the oldest and youngest blocks in the AC. It is well known that the old cratonic lithosphere contributes to continental buoyancy due to its relatively low-density (Forte & Perry, 2000; Jordan, 1978), a result from iron depletion (Goes & Van der Lee, 2002; Griffin et al., 1999). One possible contribution to the large *S*-wave variation observed in Figure 19, could be that older cratons are more depleted in iron than younger ones (Griffin et al., 1999). Iron depletion simultaneously increases β and decreases ρ, thereby potentially contributing to the observed *S*-wave anomaly, but likely not sufficiently to explain a 4% velocity anomaly (Goes et al., 2000). An alternative explanation of this trend in cratonic *S*-velocity anomaly and lithospheric thickness (Figure 19) is that the SCL of the AC was relatively recently modified by upper mantle geodynamics, such as sub-lithospheric convection or interaction with a mobile and deformable asthenosphere that is also facilitating South America's rapid westward plate motion. For example, sub-lithospheric mantle flow could heat the lithosphere of the geochronological provinces of the AC from the
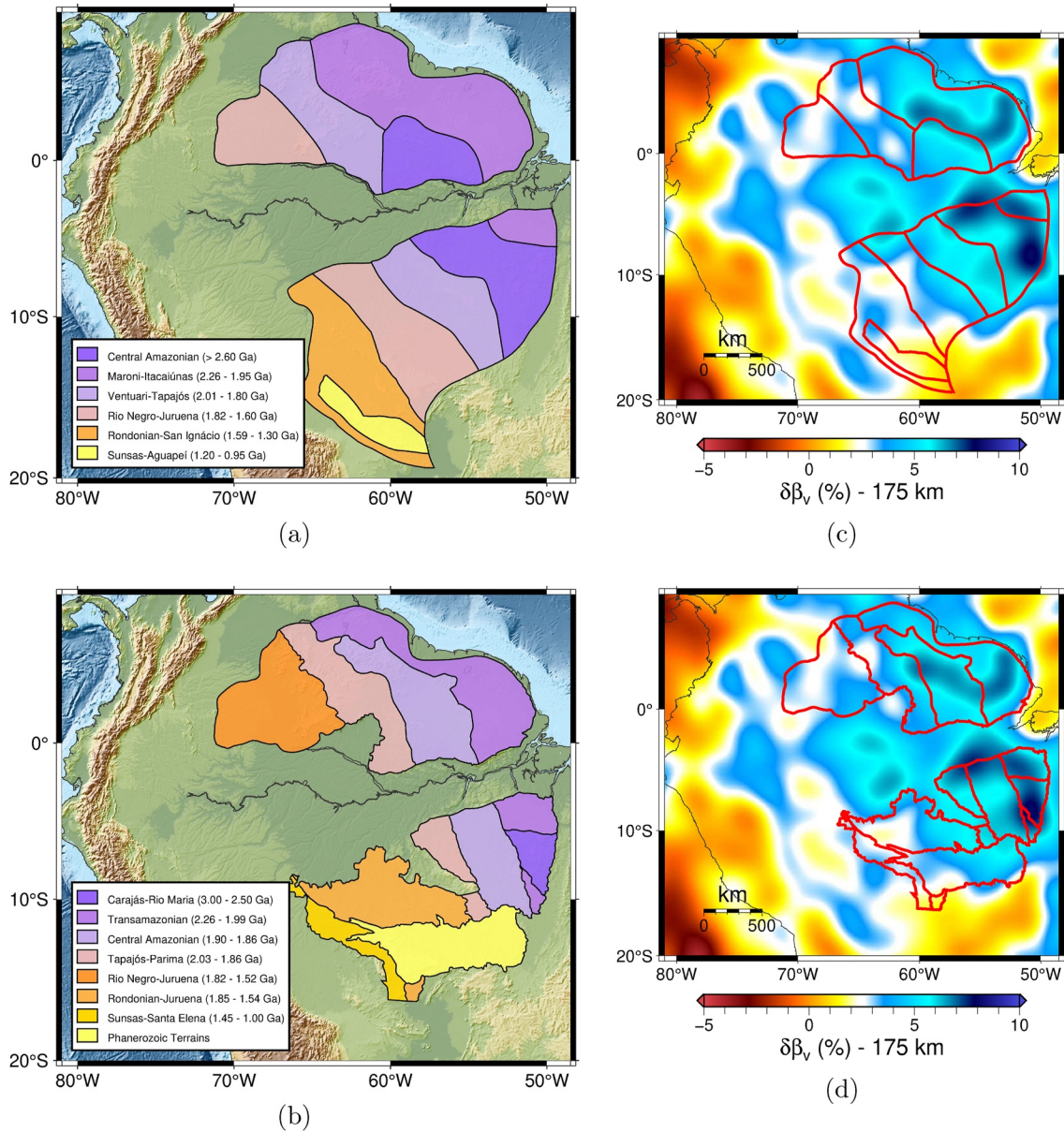
Figure 18. (a) AC geochronological provinces of Model 1 (Teixeira et al., 2019); (b) β_v anomaly at 175 km depth with the contours of model 1; (c) Amazonian geochronological Model 2 (Santos, 2003; Vasquez et al., 2008); (d) β_v anomaly at 175 km depth with the contours of model 2.

west, which would explain the trend in Figure 19 as heating from west to east rather than cooling from young to old. Finger et al. (2021) advanced a similar hypothesis after combining new seismic data with gravity data and mineral physics constraints to develop self-consistent models of temperature, composition, and density of the South American lithospheric and sub-lithospheric upper mantle. They found temperature differences from W to E ranging from 200°C to 300°C, which are consistent with the LAB depth variations observed in Figures 17 and 19. At the northwestern AC, temperatures ranging between 1,200°C and above 1,400°C for depths of 150 and 200 km, respectively, indicate that the cratonic root could have been eroded from below, possibly by upwelling of hot mantle material under the Guyana highlands (Finger et al., 2021), consistent with our observed trend of lithospheric thinning towards the west. Another hypothesis for the increasingly thicker lithospheric keels with age is the lithospheric doubling model of Vlaar (1989) and Perchuk et al. (2020) where layers of buoyant, depleted mantle were more likely to form in the Archean after plume or oceanic spreading activity, and to eventually accrete below the continental lithosphere by subduction of oceanic plates.
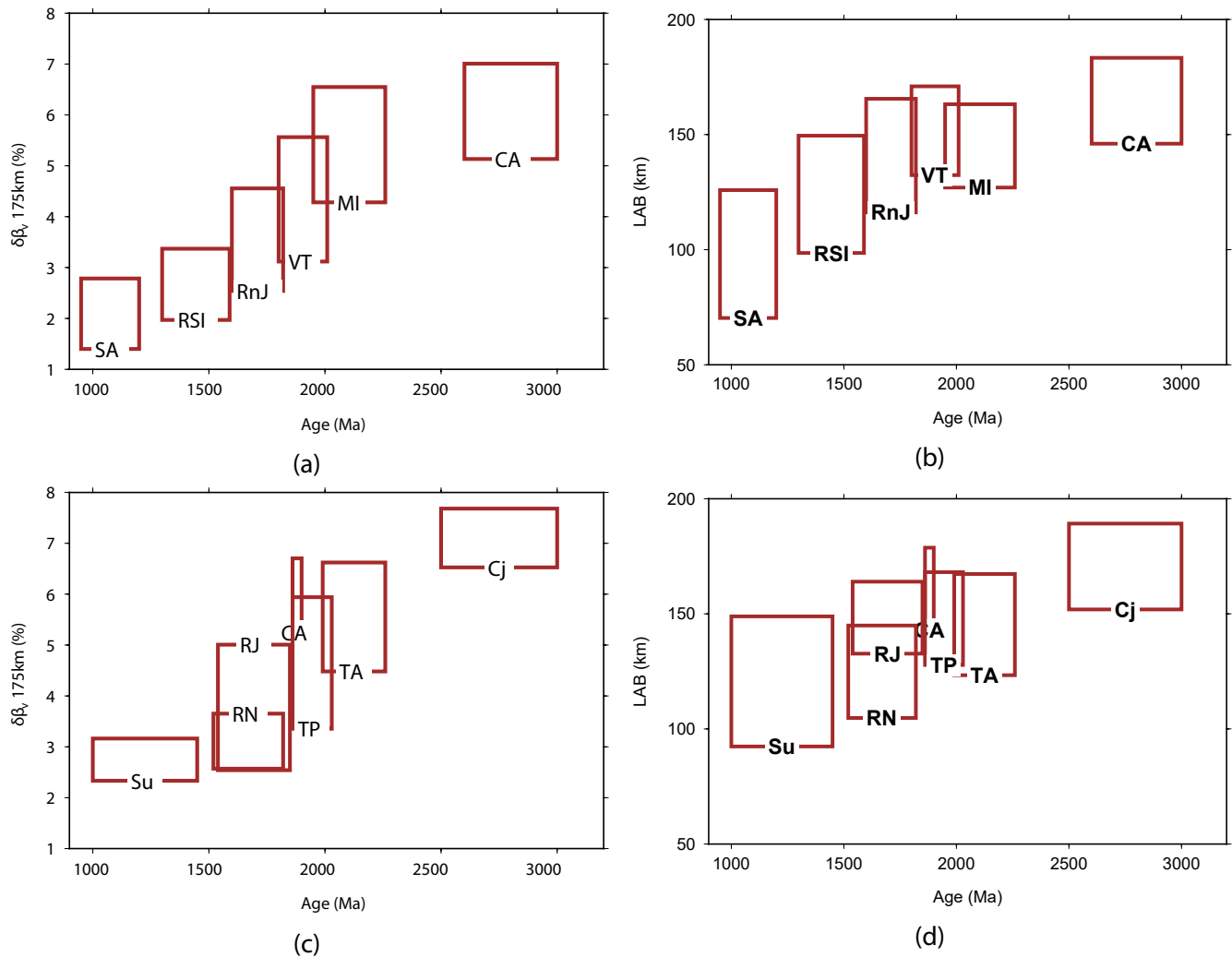
Figure 19. Correlation between age range of the Amazonian geochronological provinces (horizontal axis) and the average β_v anomaly at 175 km depth (vertical axis; plots a and c) and the LAB depth (b) and (d). The height of each box corresponds to the average anomaly ±1 standard deviation. (a) and (b) Province Model-1 Teixeira et al. (2019); (c) and (d) Province Model-2 (Santos, 2003; Vasquez et al., 2008).

Besides the E-W variations, the AC may also show differences between the two shields on both sides of the Amazon Basin. Our SAAM23 model shows reduced high-velocity anomalies beneath the Amazon Basin, east of 60°W (Figure 12) as in Heintz et al. (2005), suggesting that the rifting episode responsible for the formation of the Amazon Basin has involved heating a significant portion of the lithosphere. This reduced velocity in the eastern part of the Amazon Basin correlates with large bodies of igneous intrusions in the lower crust detected by gravity modelling and interpreted as having a Paleozoic origin (Nunn & Aires, 1988).

6. Conclusions

We constructed an adjoint tomographic model, SAAM23, based on 3D spectral-element simulations of wave propagation for the South American continent using data from 112 earthquakes recorded by 1,311 seismic stations. The model results from 23 conjugate gradient iterations where we assimilated three-component data, including both body and surface waves in the inversion. During the construction of the model, we used the EP misfit proposed by Yuan et al. (2020), a variant of the instantaneous phase misfit (Bozdağ et al., 2011), to better take scattered waves into account while effectively mitigating the cycle skip potential of phase measurements.

At long wavelengths, SAAM23 is compatible with previous seismic-tomographic studies. Well resolved is the lithosphere of cratonic nuclei in the stable platform (Amazonian and São Francisco) as well as that of the Parana-panema and Parnaíba cratonic blocks beneath sedimentary rock cover. The subducting Nazca Slab is imaged into the lower mantle and is shown to be continuous in the 300–500 km depth range down-dip from the Peruvian flat-slab segment. The slab traverses the mantle transition zone and dips into the lower mantle beneath the northern portion of South America. In the central and southern part of South America, the slab somewhat flattens near the 650 km discontinuity before straightening down-dip and continuing into the lower mantle.

Lithospheric thicknesses estimated from published *S*-wave receiver functions agree well with our LAB estimated using the most significant negative velocity gradient with depth in SAAM23. Our LAB depths show correlate with the thermal model of Finger et al. (2021). We additionally found a correlation between the average age of the geochronological provinces in the AC and increasing positive lithospheric β_v anomalies of SAAM23. Despite different formation ages, the fact that these ages are all Precambrian rules out that these differences in lithospheric structure are the result of simple cooling histories. Instead, we suggest that different degrees of iron depletion, potentially accompanied by Precambrian lithospheric doubling, could account for some of the inter-provincial differences in β_v and that westwards thinning of the lithosphere might be related to vigorous asthenospheric flow and its interaction with spatio-temporally changing mantle wedge behavior on the western margin of the continent (in response to spatio-temporal changes in shallow subduction dip angles). Like previous tomographic studies, we found no high-velocity anomalies beneath the Río de la Plata Craton. Our continental-scale, high-resolution, deeply extending, waveform based, new tomographic model, SAAM23, provides a comprehensive and robust basis for further studies of the evolution of the South American Plate.

Data Availability Statement

We downloaded the waveforms using the ObsPy (Beyreuther et al., 2010) implementation of FDSN (Berry, 1988; Romanowicz, 1990; Romanowicz et al., 1987) including stations from the networks: 2B (Heit et al., 2007), 8G (Meltzer & Beck, 2016), 9A (GEOFON Program and GFZ-Potsdam, 2007), AI (Istituto Nazionale di Oceanografia e di Geofisica Sperimentale, 1992), AY (Bureau of Mines and Energy [Haiti], 2010), BL (Institute of Astronomy, Geophysics, and Atmospheric Sciences, University of São Paulo, 1988), BR (University of Brasília, 1995), C (Universidad de Chile, 1991), C1 (Universidad de Chile, 2013), CM (INGEOMINAS - Servicio Geologico Colombiano [SGC Colombia] 1993), CU (Albuquerque Seismological Laboratory [ASL]/USGS, 2006), CW (National Centre for Seismological Research [CENAIS Cuba], 1998), CX (GFZ German Research Centre for Geosciences & Institut des Sciences de l'Univers-Centre National de la Recherche CNRS-INSU, 2006), CY (Cayman Islands Government, 2006), DR (National Seismological Centre of Autonomous University of Santo Domingo, 1998), EC (Instituto Geofisico Escuela Politecnica Nacional [IG-EPN Ecuador], 2002), G (Institut de Physique du Globe de Paris [IPGP] & et Observatoire des Sciences de la Terre de Strasbourg [EOST], 1982), GE (GEOFON Data Centre, 1993), GL (IPGP, 1950), GT (Albuquerque Seismological Laboratory [ASL]/ USGS, 1993), II (Scripps Institution of Oceanography, 1986), IQ (Cesca et al., 2009), IU (Albuquerque Seismological Laboratory [ASL]/USGS, 1988), JM (University of the West Indies Mona [Jamaica], 1985), MQ (Institut de Physique du Globe de Paris [IPGP], 1935), NA (KNMI, 2006), NB (Universidade Federal do Rio Grande do Norte, 2006), NU (Instituto Nicaraguense de Estudios Territoriales [INETER], 1975), ON (Observatório Nacional, Rio de Janeiro, 2011), OV (Protti, 1984), PA (Red Sismica Volcan Baru, 2000), PR (Rico, 1986), TC (Universidad de Costa Rica, 2017), TO (MASE, 2007), VE (Fundación Venezolana de Investigaciones Sismológicas [FUNVISIS], Caracas, 2000), WC (Meteorologische Dienst Curacao, 2006), WI (IPGP, 2008), X1 (University of Liverpool, 2007), X6 (Sandvol & Brown, 2007), XB (Wiens, 1997), XC (Institute of Astronomy, Geophysics, and Atmospheric Sciences, University of São Paulo, 2016), XE (Silver et al., 1994), XH (Zandt, 1996), XJ (University of Cambridge [UK] Earth Sciences, 2004), XN (Levander, 2008), XP (West and Christensen, 2010), XS (Vilotte & RESIF, 2011), XT (Vernon et al., 2003), XY (Schwartz, 1999), Y4 (Institute of Astronomy, Geophysics, and Atmospheric Sciences, University of São Paulo, 2013), YC (Beck et al., 2000), YH (University of Oregon, 1999), YJ (Russo, 2004), YO (Abers & Fischer, 2003), YS (Pritchard, 2009), YW (University of Bristol [UK], 2002), YZ (Schwartz et al., 2009), ZA (GEOFON Program and GFZ-Potsdam, 1994), ZB (GEOFON Program and GFZ-Potsdam, 1997), ZC (Pulliam, 2013), ZD (Wagner et al.,2010), ZE (Haberland et al., 1996), ZG (Beck et al.,2010), ZL (Beck & Zandt, 2007), ZP (GEOFON Program and GFZ-Potsdam, 1999), and ZQ (GEOFON Program and GFZ-Potsdam, 2004). The window selection and EP measurements were carried out

using PyWinAdjoint (Ciardelli, 2021), available at https://doi.org/10.5281/zenodo.4920792. Maps were created using the Oxford SubMachine tool (Hosseini et al., 2018) and GMT6 (Wessel et al., 2019).

References

Abers, G. A., & Fischer, K. M. (2003). *Broadband tomography under Costa Rica and Nicaragua*. International Federation of Digital Seismograph Networks. https://doi.org/10.7914/SN/YO_2003

Affonso, G., Rocha, M., Costa, I., Assumpção, M., Fuck, R., Albuquerque, D., et al. (2021). Lithospheric architecture of the Paranapanema block and adjacent nuclei using multiple-frequency P-wave seismic tomography. *Journal of Geophysical Research: Solid Earth*, *126*(4), e2020JB021183. https://doi.org/10.1029/2020JB021183

Albuquerque Seismological Laboratory (ASL)/USGS. (1988). *Global Seismograph Network (GSN – IRIS/USGS)*. International Federation of Digital Seismograph Networks. https://doi.org/10.7914/SN/IU

Albuquerque Seismological Laboratory (ASL)/USGS. (1993). *Global Telemetered Seismograph Network (USAF/USGS)*. International Federation of Digital Seismograph Networks. https://doi.org/10.7914/SN/GT

Albuquerque Seismological Laboratory (ASL)/USGS. (2006). *Caribbean USGS Network*. International Federation of Digital Seismograph Networks. https://doi.org/10.7914/SN/CU

Amaru, M. (2007). *Global travel time tomography with 3-D reference models* (Vol. 274). Utrecht University.

Artemieva, I. M., & Mooney, W. D. (2001). Thermal thickness and evolution of Precambrian lithosphere: A global study. *Journal of Geophysical Research: Solid Earth*, *106*(B8), 16387–16414. https://doi.org/10.1029/2000JB900439

Assumpção, M., Schimmel, M., Escalante, C., Roberto Barbosa, J., Rocha, M., & Barros, L. V. (2004). Intraplate seismicity in se Brazil: Stress concentration in lithospheric thin spots. *Geophysical Journal International*, *159*(1), 390–399. https://doi.org/10.1111/j.1365-246X.2004.02357.x

Babuska, V., & Cara, M. (1991). *Seismic anisotropy in the Earth* (Vol. 10). Springer Science + Business Media.

Beck, S., Wallace, T., & Zandt, G. (2000). *Slab geometry in the southern Andes*. International Federation of Digital Seismograph Networks. https://doi.org/10.7914/SN/YC_2000

Beck, S., & Zandt, G. (2007). *Lithospheric structure and deformation of the flat slab region of Argentina*. International Federation of Digital Seismograph Networks. https://doi.org/10.7914/SN/ZL_2007

Beck, S., Zandt, G., & Wagner, L. (2010). *Central Andean uplift and the geodynamics of the high topography*. International Federation of Digital Seismograph Networks. https://doi.org/10.7914/SN/ZG_2010

Beller, S., Monteiller, V., Operto, S., Nolet, G., Paul, A., & Zhao, L. (2018). Lithospheric architecture of the South-Western Alps revealed by multiparameter teleseismic full-waveform inversion. *Geophysical Journal International*, *212*(2), 1369–1388. https://doi.org/10.1093/gji/ggx216

Berry, M. J. (1988). *The federation of digital seismographic networks*. Paper presented at the Workshop on downhole seismometers in the deep ocean at woods hole oceanographic institution. Retrieved from https://www.fdsn.org/publications/historical/

Beyreuther, M., Barsch, R., Krischer, L., Megies, T., Behr, Y., & Wassermann, J. (2010). ObsPy: A Python toolbox for seismology. *Seismological Research Letters*, *81*(3), 530–533. https://doi.org/10.1785/gssrl.81.3.530

Bianchi, M. B., Assumpção, M., Koch, C., & Beck, S. (2021). Effect of the cold nazca slab on the depth of the 660 km discontinuity in south America. *Journal of South American Earth Sciences*, *112*, 103607. https://doi.org/10.1016/j.jsames.2021.103607

Bianchi, M. B., Assumpção, M., Rocha, M. P., Carvalho, J. M., Azevedo, P. A., Fontes, S. L., et al. (2018). The Brazilian Seismographic Network (RSBR): Improving seismic monitoring in Brazil. *Seismological Research Letters*, *89*(2A), 452–457. https://doi.org/10.1785/0220170227

Blanco, J. F., Vargas, C. A., & Monsalve, G. (2017). Lithospheric thickness estimation beneath Northwestern South America from an S-wave receiver function analysis. *Geochemistry, Geophysics, Geosystems*, *18*(4), 1376–1387. https://doi.org/10.1002/2016GC006785

Blom, N., Gokhberg, A., & Fichtner, A. (2020). Seismic waveform tomography of the central and eastern Mediterranean upper mantle. *Solid Earth*, *11*(2), 669–690. https://doi.org/10.5194/se-11-669-2020

Bozdağ, E., Peter, D., Lefebvre, M., Komatitsch, D., Tromp, J., Hill, J., et al. (2016). Global adjoint tomography: First-generation model. *Geophysical Journal International*, *207*(3), 1739–1766. https://doi.org/10.1093/gji/ggw356

Bozdağ, E., Trampert, J., & Tromp, J. (2011). Misfit functions for full waveform inversion based on instantaneous phase and envelope measurements. *Geophysical Journal International*, *185*(2), 845–870. https://doi.org/10.1111/j.1365-246X.2011.04970.x

de Brito Neves, B. B., & Fuck, R. A. (2014). The basement of the South American platform: Half Laurentian (N-NW)+ half Gondwanan (E-SE) domains. *Precambrian Research*, *244*, 75–86. https://doi.org/10.1016/j.precamres.2013.09.020

Brossier, R., Operto, S., & Virieux, J. (2010). Which data residual norm for robust elastic frequency-domain full waveform inversion? *Geophysics*, *75*(3), R37–R46. https://doi.org/10.1190/1.3379323

Buland, R., & Chapman, C. (1983). The computation of seismic travel times. *Bulletin of the Seismological Society of America*, *73*(5), 1271–1302. https://doi.org/10.1785/BSSA0730051271

Bunks, C., Saleck, F. M., Zaleski, S., & Chavent, G. (1995). Multiscale seismic waveform inversion. *Geophysics*, *60*(5), 1457–1473. https://doi.org/10.1190/1.1443880

Bureau of Mines and Energy (Haiti). (2010). *Haitian Seismic Network*. International Federation of Digital Seismograph Networks.

Capdeville, Y., Chaljub, E., & Montagner, J. P. (2003). Coupling the spectral element method with a modal solution for elastic wave propagation in global earth models. *Geophysical Journal International*, *152*(1), 34–67. https://doi.org/10.1046/j.1365-246X.2003.01808.x

Cayman Islands Government. (2006). *Cayman Islands*. International Federation of Digital Seismograph Networks.

Celli, N., Lebedev, S., Schaeffer, A., Ravenna, M., & Gaina, C. (2020). The upper mantle beneath the South Atlantic Ocean, South America and Africa from waveform tomography with massive data sets. *Geophysical Journal International*, *221*(1), 178–204. https://doi.org/10.1093/gji/ggz574

Cervenỳ, V. (2001). *Seismic ray theory* (Vol. 110). Cambridge University Press. https://doi.org/10.1007/0-387-30752-4_134

Cesca, S., Sobiesiak, M., Tassara, A., Olcay, M., Günther, E., Mikulla, S., et al. (2009). *The Iquique Local Network and PicArray*. GFZ Data Services. https://doi.org/10.14470/vd070092

Chaljub, E., Capdeville, Y., & Vilotte, J.-P. (2003). Solving elastodynamics in a fluid–solid heterogeneous sphere: A parallel spectral element approximation on non-conforming grids. *Journal of Computational Physics*, *187*(2), 457–491. https://doi.org/10.1016/S0021-9991(03)00119-0

Chaljub, E., & Valette, B. (2004). Spectral element modelling of three-dimensional wave propagation in a self-gravitating Earth with an arbitrarily stratified outer core. *Geophysical Journal International*, *158*(1), 131–141. https://doi.org/10.1111/j.1365-246X.2004.02267.x

Chamani, M. (2020). O Lineamento Transbrasiliano: Um elemento chave na evoluçã da Plataforma Sul-Americana. In A. Bartorelli, W. Teixeira, & B. B. de Brito Neves (Eds.), *Geocronologia e Evolução Tectônica do Continente Sul-Americano: A contribuição de Umberto Giuseppe Cordani* (pp. 181–202). Solaris Edições Culturais.

Chen, Y.-W., Hill, J., Lei, W., Lefebvre, M., Tromp, J., Bozdag, E., & Komatitsch, D. (2017). Automated time-window selection based on machine learning for full-waveform inversion. In *SEG technical program expanded abstracts 2017* (pp. 1604–1609). Society of Exploration Geophysicists. https://doi.org/10.1190/segam2017-17734162.1

Chen, Y.-W., Wu, J., & Suppe, J. (2019). Southward propagation of nazca subduction along the Andes. *Nature*, *565*(7740), 441–447. https://doi.org/10.1038/s41586-018-0860-1

Ciardelli, C. (2021). *caiociardelli/pywinadjoint: v1.0.0-alpha*. Zenodo. https://doi.org/10.5281/zenodo.5172215

Cordani, U. G., de Brito Neves, B. B., & Thomaz Filho, A. (2009). Estudo preliminar de Integração do Pré-Cambriano com os Eventos tectônicos das Bacias Sedimentares Brasileiras (Atualização). *Boletim de Geociencias da Petrobras, Rio de Janeiro*, *17*(1), 205–219.

Cordani, U. G., Milani, E. J., Thomaz Filho, A., & Campos, D. A. (2000). *Tectonic Evolution of South America*. Retrieved from http://rigeo.cprm.gov.br/jspui/handle/doc/19419

Cordani, U. G., Sato, K., Sproessner, W., & Fernandes, F. S. (2016). U-Pb zircon ages of rocks from the Amazonas Territory of Colombia and their bearing on the tectonic history of the NW sector of the Amazonian Craton. *Brazilian Journal of Geology*, *46*, 5–35. https://doi.org/10.1590/2317-4889201620150012

Cordani, U. G., & Teixeira, W. (2007). Proterozoic accretionary belts in the amazonian craton. *Geological Society of America Memoirs*, *200*, 297–320. https://doi.org/10.1130/2007.1200(14)

Cordani, U. G., Teixeira, W., D'Agrella-Filho, M. S., & Trindade, R. I. F. (2009). The position of the Amazonian craton in supercontinents. *Gondwana Research*, *15*(3–4), 396–407. https://doi.org/10.1016/j.gr.2008.12.005

Costa, I. S. L., Rocha, M. P., Klein, E. L., & Vasquez, M. L. (2020). Lithospheric structure of the southern amazonian craton from multiple-frequency seismic tomography: Preliminary insights on tectonic and metallogenic implications. *Journal of South American Earth Sciences*, *101*, 102608. https://doi.org/10.1016/j.jsames.2020.102608

COUTINHO, Maria Glícia da Nóbrega. (2008). *Província Mineral do Tapajós: Geologia, metalogenia e mapa previsional para ouro em SIG*. CPRM.

Cowling, T. G. (1941). The non-radial oscillations of polytropic stars. *Monthly Notices of the Royal Astronomical Society*, *101*, 367–375. https://doi.org/10.1093/mnras/101.8.367

Crotwell, H. P., Owens, T. J., & Ritsema, J. (1999). The TauP toolkit: Flexible seismic travel-time and ray-path utilities. *Seismological Research Letters*, *70*(2), 154–160. https://doi.org/10.1785/gssrl.70.2.154

Dahlen, F., Hung, S.-H., & Nolet, G. (2000). Fréchet kernels for finite-frequency traveltimes-I. Theory. *Geophysical Journal International*, *141*(1), 157–174. https://doi.org/10.1046/j.1365-246X.2000.00070.x

Dahlen, F., & Zhou, Y. (2006). Surface-wave group-delay and attenuation kernels. *Geophysical Journal International*, *165*(2), 545–554. https://doi.org/10.1111/j.1365-246X.2006.02913.x

de Almeida, F. F. M., de Brito Neves, B. B., & Carneiro, C. D. R. (2000). The origin and evolution of the South American Platform. *Earth-Science Reviews*, *50*(1–2), 77–111. https://doi.org/10.1016/S0012-8252(99)00072-0

Debye, P. (1909). Näherungsformeln für die Zylinderfunktionen für große Werte des Arguments und unbeschränkt veränderliche Werte des Index. *Mathematische Annalen*, *67*(4), 535–558. https://doi.org/10.1007/bf01450097

Dziewonski, A., Chou, T.-A., & Woodhouse, J. H. (1981). Determination of earthquake source parameters from waveform data for studies of global and regional seismicity. *Journal of Geophysical Research*, *86*(B4), 2825–2852. https://doi.org/10.1029/JB086iB04p02825

Ekström, G., Nettles, M., & Dziewoński, A. (2012). The global CMT project 2004–2010: Centroid-moment tensors for 13,017 earthquakes. *Physics of the Earth and Planetary Interiors*, *200*, 1–9. https://doi.org/10.1016/j.pepi.2012.04.002

Feng, M., Assumpçao, M., & Van der Lee, S. (2004). Group-velocity tomography and lithospheric S-velocity structure of the South American continent. *Physics of the Earth and Planetary Interiors*, *147*(4), 315–331. https://doi.org/10.1016/j.pepi.2004.07.008

Feng, M., Van der Lee, S., & Assumpção, M. (2007). Upper mantle structure of South America from joint inversion of waveforms and fundamental mode group velocities of Rayleigh waves. *Journal of Geophysical Research*, *112*(B4). https://doi.org/10.1029/2006JB004449

Fichtner, A. (2010). *Full seismic waveform modelling and inversion*. Springer Science + Business Media.

Fichtner, A., Bunge, H.-P., & Igel, H. (2006). The adjoint method in seismology: I. Theory. *Physics of the Earth and Planetary Interiors*, *157*(1–2), 86–104. https://doi.org/10.1016/j.pepi.2006.03.016

Fichtner, A., Kennett, B. L. N., Igel, H., & Bunge, H.-P. (2009). Full seismic waveform tomography for upper-mantle structure in the Australasian region using adjoint methods. *Geophysical Journal International*, *179*(3), 1703–1725. https://doi.org/10.1111/j.1365-246X.2009.04368.x

Fichtner, A., & Trampert, J. (2011). Resolution analysis in full waveform inversion. *Geophysical Journal International*, *187*(3), 1604–1624. https://doi.org/10.1111/j.1365-246X.2011.05218.x

Finger, N.-P., Kaban, M., Tesauro, M., Haeger, C., Mooney, W., & Thomas, M. (2021). A thermo-compositional model of the cratonic lithosphere of South America. *Geochemistry, Geophysics, Geosystems*, *22*(4), e2020GC009307. https://doi.org/10.1029/2020GC009307

Fletcher, R., & Reeves, C. M. (1964). Function minimization by conjugate gradients. *The Computer Journal*, *7*(2), 149–154. https://doi.org/10.1093/comjnl/7.2.149

Forte, A. M., & Perry, H. C. (2000). Geodynamic evidence for a chemically depleted continental tectosphere. *Science*, *290*(5498), 1940–1944. https://doi.org/10.1126/science.290.5498.1940

French, S. W., & Romanowicz, B. (2015). Broad plumes rooted at the base of the Earth's mantle beneath major hotspots. *Nature*, *525*(7567), 95–99. https://doi.org/10.1038/nature14876

Fukao, Y., Obayashi, M., Inoue, H., & Nenbai, M. (1992). Subducting slabs stagnant in the mantle transition zone. *Journal of Geophysical Research: Solid Earth*, *97*(B4), 4809–4822. https://doi.org/10.1029/91JB02749

Fundación Venezolana de Investigaciones Sismológicas (FUNVISIS), Caracas. (2000). *Red Sismológica Satelital Nacional*. International Federation of Digital Seismograph Networks. https://doi.org/10.7914/SN/VE

Gao, Y., Tilmann, F., van Herwaarden, D.-P., Thrastarson, S., Fichtner, A., Heit, B., et al. (2021). Full waveform inversion beneath the Central Andes: Insight into the dehydration of the Nazca slab and delamination of the back-arc lithosphere. *Journal of Geophysical Research: Solid Earth*, *126*(7), e2021JB021984. https://doi.org/10.1029/2021JB021984

GEOFON Data Centre. (1993). *GEOFON Seismic Network*. Deutsches GeoForschungsZentrum GFZ. https://doi.org/10.14470/tr560404

GEOFON Program and Gfz-Potsdam, G. (1994). *PISCO94 PS (PISCO94)*. International Federation of Digital Seismograph Networks.

GEOFON Program and GFZ-Potsdam, G. (1997). *PUNA97*. International Federation of Digital Seismograph Networks.

GEOFON Program and GFZ-Potsdam, G. (1999). *ISSA*. International Federation of Digital Seismograph Networks.

GEOFON Program and GFZ-Potsdam, G. (2004). *Cerro Blanco*. International Federation of Digital Seismograph Networks.

GEOFON Program and GFZ-Potsdam, G. (2007). *COBO. International Federation of Digital Seismograph Networks*.

GFZ German Research Centre for Geosciences & Institut des Sciences de l'Univers-Centre National de la Recherche CNRS-INSU. (2006). *IPOC Seismic Network*. Integrated Plate Boundary Observatory Chile—IPOC. https://doi.org/10.14470/pk615318

Goes, S., Govers, R., & Vacher, P. (2000). Shallow mantle temperatures under Europe from P and S wave tomography. *Journal of Geophysical Research: Solid Earth*, *105*(B5), 11153–11169. https://doi.org/10.1029/1999JB900300

Goes, S., & van der Lee, S. (2002). Thermal structure of the North American uppermost mantle inferred from seismic tomography. *Journal of Geophysical Research: Solid Earth*, *107*(B3). ETG–2. https://doi.org/10.1029/2000jb000049

Grand, S. P. (1987). Tomographic inversion for shear velocity beneath the North American plate. *Journal of Geophysical Research: Solid Earth*, *92*(B13), 14065–14090. https://doi.org/10.1029/JB092iB13p14065

Griffin, W., O'Reilly, S. Y., & Ryan, C. (1999). *The composition and origin of sub-continental lithospheric mantle*. The Geochemical Society, Special Publication.

Haberland, C., Rietbrock, A., Asch, G., & Chong, G. (1996). *The ANCORP Seismic Network*. GFZ Data Services. https://doi.org/10.14470/mr6441682066

Hayes, G. P., Moore, G. L., Portner, D. E., Hearne, M., Flamme, H., Furtney, M., et al. (2018). Slab2, a comprehensive subduction zone geometry model. *Science*, *362*(6410), 58–61. https://doi.org/10.1126/science.aat4723

Hayes, G. P., Smoczyk, G. M., Benz, H. M., VillaseSñor, A., & Furlong, K. P. (2015). *Seismicity of the Earth 1900–2013: Seismotectonics of South America (Nazca Plate Region)*. Open-File Report 2015-1031–E, 1 sheet, scale 1:14,000,000. U.S. Geological Survey. https://doi.org/10.3133/ofr20151031E

Heilbron, M., D'Agrella-Filho, M., & Alkmim, F. F. (2016). *São Francisco Craton, Eastern Brazil: Tectonic genealogy of a miniature continent*. Springer.

Heintz, M., Debayle, E., & Vauchez, A. (2005). Upper mantle structure of the South American continent and neighboring oceans from surface wave tomography. *Tectonophysics*, *406*(1–2), 115–139. https://doi.org/10.1016/j.tecto.2005.05.006

Heit, B., Sodoudi, F., Yuan, X., Bianchi, M., & Kind, R. (2007). An S receiver function analysis of the lithospheric structure in South America. *Geophysical Research Letters*, *34*(14). https://doi.org/10.1029/2007GL030317

Heit, B., Yuan, X., Bianchi, M., Sodoudi, F., & Kind, R. (2008). Crustal thickness estimation beneath the southern central Andes at 30 S and 36 S from S wave receiver function analysis. *Geophysical Journal International*, *174*(1), 249–254. https://doi.org/10.1111/j.1365-246X.2008.03780.x

Heit, B., Yuan, X., Kind, R., & Asch, G. (2007). *Lithospheric dynamics in the Southernmost Andean plateau (PUDEL)*. Deutsches GeoForschungsZentrum GFZ. https://doi.org/10.14470/7o092361

Hosseini, K., Matthews, K. J., Sigloch, K., Shephard, G. E., Domeier, M., & Tsekhmistrenko, M. (2018). SubMachine: Web-based tools for exploring seismic tomography and other models of Earth's deep interior. *Geochemistry, Geophysics, Geosystems*, *19*(5), 1464–1483. https://doi.org/10.1029/2018GC007431

Hosseini, K., Sigloch, K., Tsekhmistrenko, M., Zaheri, A., Nissen-Meyer, T., & Igel, H. (2020). Global mantle structure from multifrequency tomography using P, PP and P-diffracted waves. *Geophysical Journal International*, *220*(1), 96–141. https://doi.org/10.1093/gji/ggz394

INGEOMINAS - Servicio Geologico Colombiano (SGC Colombia). (1993). *Red Sismologica Nacional de Colombia*. International Federation of Digital Seismograph Networks. https://doi.org/10.7914/SN/CM

Inoue, H., Fukao, Y., Tanabe, K., & Ogata, Y. (1990). Whole mantle P-wave travel time tomography. *Physics of the Earth and Planetary Interiors*, *59*(4), 294–328. https://doi.org/10.1016/0031-9201(90)90236-Q

Institute of Astronomy, Geophysics, and Atmospheric Sciences, University of São Paulo. (1988). *Brazilian Lithospheric Seismic Project (BLSP)*. International Federation of Digital Seismograph Networks.

Institute of Astronomy, Geophysics, and Atmospheric Sciences, University of São Paulo. (2013). *Brazilian Temporary Seismographic Experiments*. International Federation of Digital Seismograph Networks.

Institute of Astronomy, Geophysics, and Atmospheric Sciences, University of São Paulo. (2016). *Pantanal, Chaco and Paraná (PCPB) Structural Studies Network (PCPB)*. International Federation of Digital Seismograph Networks.

Instituto Geofisico Escuela Politecnica Nacional (IG-EPN Ecuador). (2002). *Ecuador Seismic Network*. International Federation of Digital Seismograph Networks.

Istituto Nazionale di Oceanografia e di Geofisica Sperimentale. (1992). *Antarctic Seismographic Argentinean Italian Network – OGS*. International Federation of Digital Seismograph Networks. https://doi.org/10.7914/SN/AI

Instituto Nicaraguense de Estudios Territoriales (INETER). (1975). *Nicaraguan Seismic Network*. International Federation of Digital Seismograph Networks. https://doi.org/10.7914/SN/NU

Institut de Physique du Globe de Paris (IPGP). (1935). *Martinique Seismic and Volcano Observatory Network (OVSM)*. International Federation of Digital Seismograph Networks.

Institut de Physique du Globe de Paris (IPGP). (1950). *Guadeloupe Seismic and Volcano Observatory Network (OVSG)*. International Federation of Digital Seismograph Networks.

Institut de Physique du Globe de Paris (IPGP). (2008). *GNSS, seismic broadband and strong motion permanent networks in West Indies*. Institut de Physique du Globe de Paris. https://doi.org/10.18715/antilles.wi

Institut de Physique du Globe de Paris (IPGP) & et Observatoire des Sciences de la Terre de Strasbourg (EOST). (1982). *GEOSCOPE, French Global Network of broad band seismic stations*. Institut de physique du globe de Paris, Université de Paris. https://doi.org/10.18715/geoscope.g

James, D. E., & Snoke, J. A. (1990). Seismic evidence for continuity of the deep slab beneath central and eastern Peru. *Journal of Geophysical Research*, *95*(B4), 4989–5001. https://doi.org/10.1029/JB095iB04p04989

Johansson, Å., Bingen, B., Huhma, H., Waight, T., Vestergaard, R., Soesoo, A., et al. (2021). *A geochronological review of magmatism along the external margin of Columbia and in the Grenville-age orogens forming the core of Rodinia*. Precambrian Research. https://doi.org/10.1016/j.precamres.2021.106463

Johnston, A., Coppersmith, K., Kanter, L., & Cornell, C. (1994). *The earthquakes of stable continental regions: Assessment of large earthquake potential*. EPRI Report. TR-102261.

Jordan, T. H. (1978). Composition and development of the continental tectosphere. *Nature*, *274*(5671), 544–548. https://doi.org/10.1038/274544a0

Kawakatsu, H. (2016). A new fifth parameter for transverse isotropy. *Geophysical Journal International*, *204*(1), 682–685. https://doi.org/10.1093/gji/ggv479

Kennett, B. L., Engdahl, E., & Buland, R. (1995). Constraints on seismic velocities in the Earth from traveltimes. *Geophysical Journal International*, *122*(1), 108–124. https://doi.org/10.1111/j.1365-246X.1995.tb03540.x

KNMI. (2006). *Caribbean Netherlands Seismic Network*. Royal Netherlands Meteorological Institute. https://doi.org/10.21944/dffa7a3f-7e3a-3b33-a436-516a01b6af3f

Komatitsch, D., & Tromp, J. (1999). Introduction to the spectral element method for three-dimensional seismic wave propagation. *Geophysical Journal International*, *139*(3), 806–822. https://doi.org/10.1046/j.1365-246x.1999.00967.x

Komatitsch, D., & Tromp, J. (2002a). Spectral-element simulations of global seismic wave propagation-II. Three-dimensional models, oceans, rotation and self-gravitation. *Geophysical Journal International*, *150*(1), 303–318. https://doi.org/10.1046/j.1365-246X.2002.01716.x

Komatitsch, D., & Tromp, J. (2002b). Spectral-element simulations of global seismic wave propagation-I. Validation. *Geophysical Journal International*, *149*(2), 390–412. https://doi.org/10.1046/j.1365-246X.2002.01653.x

Komatitsch, D., & Vilotte, J.-P. (1998). The spectral element method: An efficient tool to simulate the seismic response of 2D and 3D geological structures. *Bulletin of the Seismological Society of America*, *88*(2), 368–392

Komatitsch, D., Xie, Z., Bozdağ, E., Sales de Andrade, E., Peter, D., Liu, Q., et al. (2016). Anelastic sensitivity kernels with parsimonious storage for adjoint tomography and full waveform inversion. *Geophysical Journal International*, *206*(3), 1467–1478. https://doi.org/10.1093/gji/ggw224

Kristeková, M., Kristek, J., & Moczo, P. (2009). Time-frequency misfit and goodness-of-fit criteria for quantitative comparison of time signals. *Geophysical Journal International*, *178*(2), 813–825. https://doi.org/10.1111/j.1365-246X.2009.04177.x

Kustowski, B., Ekström, G., & Dziewoński, A. (2008). Anisotropic shear-wave velocity structure of the Earth's mantle: A global model. *Journal of Geophysical Research*, *113*(B6). https://doi.org/10.1029/2007JB005169

Laske, G., Masters, G., Ma, Z., & Pasyanos, M. (2012). CRUST1.0: An updated global model of Earth's crust. *Geophysical Research Abstracts*, *14*, 3743. https://doi.org/10.17611/DP/emccrust10

Lebedev, S., Nolet, G., Meier, T., & Van der Hilst, R. D. (2005). Automated multimode inversion of surface and S waveforms. *Geophysical Journal International*, *162*(3), 951–964. https://doi.org/10.1111/j.1365-246X.2005.02708.x

Lebedev, S., & Van der Hilst, R. D. (2008). Global upper-mantle tomography with the automated multimode inversion of surface and S-wave forms. *Geophysical Journal International*, *173*(2), 505–518. https://doi.org/10.1111/j.1365-246X.2008.03721.x

Lee, E.-J., & Chen, P. (2013). Automating seismic waveform analysis for full 3-D waveform inversions. *Geophysical Journal International*, *194*(1), 572–589. https://doi.org/10.1093/gji/ggt124

Lei, W., Ruan, Y., Bozdağ, E., Peter, D., Lefebvre, M., Komatitsch, D., et al. (2020). Global adjoint tomography-model GLAD-M25. *Geophysical Journal International*, *223*(1), 1–21. https://doi.org/10.1093/gji/ggaa253

Lekić, V., & Romanowicz, B. (2011). Inferring upper-mantle structure by full waveform tomography with the spectral element method. *Geophysical Journal International*, *185*(2), 799–831. https://doi.org/10.1111/j.1365-246X.2011.04969.x

Levander, A. (2008). *Bolivar: Western Venezuela*. International Federation of Digital Seismograph Networks. https://doi.org/10.7914/SN/XN_2008

Li, C., Van der Hilst, R. D., Engdahl, E. R., & Burdick, S. (2008). A new global model for P wave speed variations in Earth's mantle. *Geochemistry, Geophysics, Geosystems*, *9*(5). https://doi.org/10.1029/2007GC001806

Li, X.-D., & Romanowicz, B. (1995). Comparison of global waveform inversions with and without considering cross-branch modal coupling. *Geophysical Journal International*, *121*(3), 695–709. https://doi.org/10.1111/j.1365-246X.1995.tb06432.x

Li, X.-D., & Romanowicz, B. (1996). Global mantle shear velocity model developed using nonlinear asymptotic coupling theory. *Journal of Geophysical Research: Solid Earth*, *101*(B10), 22245–22272. https://doi.org/10.1029/96JB01306

Liu, K. H., Gao, S. S., Silver, P. G., & Zhang, Y. (2003). Mantle layering across central South America. *Journal of Geophysical Research: Solid Earth*, *108*(B11). https://doi.org/10.1029/2002JB002208

Liu, Q., & Gu, Y. (2012). Seismic imaging: From classical to adjoint tomography. *Tectonophysics*, *566*, 31–66. https://doi.org/10.1016/j.tecto.2012.07.006

Liu, Z., Huang, J., & Yao, H. (2016). Anisotropic Rayleigh wave tomography of Northeast China using ambient seismic noise. *Physics of the Earth and Planetary Interiors*, *256*, 37–48. https://doi.org/10.1016/j.pepi.2016.05.001

Luo, Y., Modrak, R., & Tromp, J. (2013). Strategies in adjoint tomography. In W. Freeden, M. Z. Nashed, & T. Sonar, (Eds.), *Handbook of geomathematics* (2nd ed., pp. 1943–2001). Springer. https://doi.org/10.1007/978-3-642-27793-1_96-2

Luo, Y., & Schuster, G. T. (1991). Wave-equation traveltime inversion. *Geophysics*, *56*(5), 645–653. https://doi.org/10.1190/1.1443081

Macambira, M. J. B., Teixeira, W., & Vasquez, M. L. (2020). O Cráton Amazônico e suas Províncias Geocronológicas: O Legado de Umberto Cordani. In A. Bartorelli, W. Teixeira, & B. B. de Brito Neves (Eds.), *Geocronologia e Evolução Tectônica do Continente Sul-Americano: A contribuição de Umberto Giuseppe Cordani* (pp. 46–172). Solaris Edições Culturais.

Maggi, A., Tape, C., Chen, M., Chao, D., & Tromp, J. (2009). An automated time-window selection algorithm for seismic tomography. *Geophysical Journal International*, *178*(1), 257–281. https://doi.org/10.1111/j.1365-246X.2009.04099.x

Mantovani, M., Quintas, M., Shukowsky, W., & de Brito Neves, B. (2005). Delimitation of the Paranapanema Proterozoic block: A geophysical contribution. *Episodes-Newsmagazine of the International Union of Geological Sciences*, *28*(1), 18–315. https://doi.org/10.18814/epiiugs/2005/v28i1/002

Marquering, H., Dahlen, F., & Nolet, G. (1999). Three-dimensional sensitivity kernels for finite-frequency traveltimes: The banana-doughnut paradox. *Geophysical Journal International*, *137*(3), 805–815. https://doi.org/10.1046/j.1365-246x.1999.00837.x

MASE. (2007). *Meso America subduction experiment*. Caltech. https://doi.org/10.7909/c3rn35sp

Meltzer, A., & Beck, S. (2016). *2016 Pedernales earthquake aftershock deployment Ecuador*. International Federation of Digital Seismograph Networks. https://doi.org/10.7914/SN/8G_2016

Meteorologische Dienst Curacao. (2006). *Curacao Seismic Network*. International Federation of Digital Seismograph Networks. Retrieved from http://www.fdsn.org/networks/detail/WC/

Modrak, R., & Tromp, J. (2016). Seismic waveform inversion best practices: Regional, global and exploration test cases. *Geophysical Journal International*, *206*(3), 1864–1889. https://doi.org/10.1093/gji/ggw202

Mohammadzaheri, A., Sigloch, K., Hosseini, K., & Mihalynuk, M. G. (2021). Subducted lithosphere under south America from multi-frequency P-wave tomography. *Journal of Geophysical Research: Solid Earth*, *126*, e2020JB020704. https://doi.org/10.1029/2020JB020704

Montagner, J.-P., & Anderson, D. L. (1989). Petrological constraints on seismic anisotropy. *Physics of the Earth and Planetary Interiors*, *54*(1–2), 82–105. https://doi.org/10.1016/0031-9201(89)90189-1

Montelli, R., Nolet, G., Dahlen, F., & Masters, G. (2006). A catalogue of deep mantle plumes: New results from finite-frequency tomography. *Geochemistry, Geophysics, Geosystems*, *7*(11). https://doi.org/10.1029/2006GC001248

Montelli, R., Nolet, G., Dahlen, F., Masters, G., Engdahl, E. R., & Hung, S.-H. (2004). Finite-frequency tomography reveals a variety of plumes in the mantle. *Science*, *303*(5656), 338–343. https://doi.org/10.1126/science.1092485

Morelli, A., & Dziewonski, A. M. (1993). Body wave traveltimes and a spherically symmetric P-and S-wave velocity model. *Geophysical Journal International*, *112*(2), 178–194. https://doi.org/10.1111/j.1365-246X.1993.tb01448.x

National Centre for Seismological Research (CENAIS Cuba). (1998). *Servicio Sismologico Nacional de Cuba*. International Federation of Digital Seismograph Networks. https://doi.org/10.7914/SN/CW

National Seismological Centre of Autonomous University of Santo Domingo. (1998). *Centro Nacional de Sismologia*. International Federation of Digital Seismograph Networks. https://doi.org/10.7914/SN/DR

Nocedal, J., & Wright, S. (2006). *Numerical optimization*. Springer Science + Business Media.

Nolet, G. (1990). Partitioned waveform inversion and two-dimensional structure under the network of autonomously recording seismographs. *Journal of Geophysical Research*, *95*(B6), 8499–8512. https://doi.org/10.1029/JB095iB06p08499

Nolet, G., & Dahlen, F. A. (2000). Wave front healing and the evolution of seismic delay times. *Journal of Geophysical Research: Solid Earth*, *105*(B8), 19043–19054. https://doi.org/10.1029/2000JB900161

Nunn, J. A., & Aires, J. R. (1988). Gravity anomalies and flexure of the lithosphere at the middle Amazon Basin, Brazil. *Journal of Geophysical Research: Solid Earth*, *93*(B1), 415–428. https://doi.org/10.1029/JB093iB01p00415

Obayashi, M., Yoshimitsu, J., Nolet, G., Fukao, Y., Shiobara, H., Sugioka, H., et al. (2013). Finite frequency whole mantle P wave tomography: Improvement of subducted slab images. *Geophysical Research Letters*, *40*(21), 5652–5657. https://doi.org/10.1002/2013GL057401

Observatório Nacional, Rio de Janeiro. (2011). *Rede Sismográfica do Sul e do Sudeste (RSIS)*. International Federation of Digital Seismograph Networks. https://doi.org/10.7914/SN/ON

Oyhantçabal, P., Siegesmund, S., & Wemmer, K. (2011). The Río de la Plata craton: A review of units, boundaries, ages and isotopic signature. *International Journal of Earth Sciences*, *100*(2–3), 201–220. https://doi.org/10.1007/s00531-010-0580-8

Perchuk, A. L., Gerya, T. V., Zakharov, V. S., & Griffin, W. L. (2020). Building cratonic keels in Precambrian plate tectonics. *Nature*, *586*(7829), 395–401. https://doi.org/10.1038/s41586-020-2806-7

Peter, D., Boschi, L., & Woodhouse, J. (2009). Tomographic resolution of ray and finite-frequency methods: A membrane-wave investigation. *Geophysical Journal International*, *177*(2), 624–638. https://doi.org/10.1111/j.1365-246X.2009.04098.x

Peter, D., Komatitsch, D., Luo, Y., Martin, R., Le Goff, N., Casarotti, E., et al. (2011). Forward and adjoint simulations of seismic wave propagation on fully unstructured hexahedral meshes. *Geophysical Journal International*, *186*(2), 721–739. https://doi.org/10.1111/j.1365-246X.2011.05044.x

Plessix, R.-E. (2006). A review of the adjoint-state method for computing the gradient of a functional with geophysical applications. *Geophysical Journal International*, *167*(2), 495–503. https://doi.org/10.1111/j.1365-246X.2006.02978.x

Porter, R. C., Van der Lee, S., & Whitmeyer, S. J. (2019). Synthesizing EarthScope data to constrain the thermal evolution of the continental U.S. lithosphere. *Geosphere*, *15*(6), 1722–1737. https://doi.org/10.1130/ges02000.1

Portner, D. E., Rodríguez, E. E., Beck, S., Zandt, G., Scire, A., Rocha, M. P., et al. (2020). Detailed structure of the subducted Nazca slab into the lower mantle derived from continent-scale teleseismic P wave tomography. *Journal of Geophysical Research: Solid Earth*, *125*(5), e2019JB017884. https://doi.org/10.1029/2019JB017884

Priestley, K., McKenzie, D., & Ho, T. (2018). A lithosphere-asthenosphere boundary-a global model derived from multimode surface-wave tomography and petrology. In H. Yuan, & B. Romanowicz, (Eds.), *Lithospheric discontinuities* (Vol. 111–123, pp. 111–123). American Geophysical Union. https://doi.org/10.1002/9781119249740.ch6

Pritchard, M. (2009). *The life cycle of Andean volcanoes: Combining space-based and field studies*. International Federation of Digital Seismograph Networks. https://doi.org/10.7914/SN/YS_2009

Protti, M. (1984). *Observatorio Vulcanológico y Sismológico de Costa Rica*. International Federation of Digital Seismograph Networks. https://doi.org/10.7914/SN/OV

Pulliam, J. (2013). *Greater Antilles Seismic Program*. International Federation of Digital Seismograph Networks. https://doi.org/10.7914/SN/ZC_2013

Qiao, L., Yao, H., Lai, Y.-C., Huang, B.-S., & Zhang, P. (2018). Crustal structure of Southwest China and northern Vietnam from ambient noise tomography: Implication for the large-scale material transport model in SE Tibet. *Tectonics*, *37*(5), 1492–1506. https://doi.org/10.1029/2018TC004957

Ramos, V. (1999). Plate tectonic setting of the Andean Cordillera. *Episodes*, *22*, 183–190. https://doi.org/10.18814/epiiugs/1999/v22i3/005

Ramos, V. (2004). La Plataforma Patagónica y sus relaciones con la Plataforma Brasilera. In V. Mantesso-Neto, A. Bartorelli, C. D. R. Carneiro, & B. B. de Brito Neves (Eds.), *Geologia do continente sul-americano-evolução da obra de fernando flávio marques de almeida*. (pp. 339–371). Beca Produções Culturais Limitada.

Rapela, C. W., Fanning, C. M., Casquet, C., Pankhurst, R. J., Spalletti, L., Poiré, D., & Baldo, E. G. (2011). The Rio de la Plata craton and the adjoining Pan-African/brasiliano terranes: Their origins and incorporation into south-west Gondwana. *Gondwana Research*, *20*(4), 673–690. https://doi.org/10.1016/j.gr.2011.05.001

Red Sismica Volcan Baru. (2000). *ChiriNet*. International Federation of Digital Seismograph Networks. https://doi.org/10.7914/SN/PA

Rickers, F., Fichtner, A., & Trampert, J. (2012). Imaging mantle plumes with instantaneous phase measurements of diffracted waves. *Geophysical Journal International*, *190*(1), 650–664. https://doi.org/10.1111/j.1365-246X.2012.05515.x

Rickers, F., Fichtner, A., & Trampert, J. (2013). The Iceland-jan mayen plume System and its impact on mantle dynamics in the North Atlantic region: Evidence from full-waveform inversion. *Earth and Planetary Science Letters*, *367*, 39–51. https://doi.org/10.1016/j.epsl.2013.02.022

Rico, U. O. P. (1986). *Puerto Rico seismic network and Puerto Rico strong motion Program (PRSN and PRSMP)*. International Federation of Digital Seismograph Networks.

Rivadeneyra-Vera, C., Bianchi, M., Assumpção, M., Cedraz, V., Julià, J., Rodríguez, M., et al. (2019). An updated crustal thickness map of central south America based on receiver function measurements in the region of the Chaco, Pantanal, and Paraná basins, southwestern Brazil. *Journal of Geophysical Research: Solid Earth*, *124*(8), 8491–8505. https://doi.org/10.1029/2018JB016811

Rocha, M. P, Assumpção, M., Affonso, G., Azevedo, P. A., & Bianchi, M. (2019). Teleseismic P wave tomography beneath the Pantanal, Paraná, and Chaco-Paraná basins, SE south America: Delimiting lithospheric blocks of the SW Gondwana assemblage. *Journal of Geophysical Research: Solid Earth*, *124*(7), 7120–7137. https://doi.org/10.1029/2018JB016807

Rocha, M. P., Azevedo, P. A., Assumpção, M., Pedrosa-Soares, A. C., Fuck, R., & Von Huelsen, M. G. (2019s). Delimiting the Neoproterozoic São Francisco paleocontinental block with P-wave traveltime tomography. *Geophysical Journal International*, *219*(1), 633–644. https://doi.org/10.1093/gji/ggz323

Rocha, M. P., Schimmel, M., & Assumpçao, M. (2011). Upper-mantle seismic structure beneath SE and Central Brazil from P-and S-wave regional traveltime tomography. *Geophysical Journal International*, *184*(1), 268–286. https://doi.org/10.1111/j.1365-246X.2010.04831.x

Rodríguez, E. E., Portner, D. E., Beck, S. L., Rocha, M. P., Bianchi, M. B., Assumpção, M., et al. (2021). Mantle dynamics of the Andean Subduction Zone from continent-scale teleseismic S-wave tomography. *Geophysical Journal International*, *224*(3), 1553–1571. https://doi.org/10.1093/gji/ggaa536

Romanowicz, B. (1990). *The federation of digital broad band seismic networks*. Paper presented at the Workshop on «mednet; the broadband seismic network for the mediterranean (pp. 287–300). Retrieved from https://www.fdsn.org/media/_s/publications/historical/fdsn_report_ro-manowicz.pdf

Romanowicz, B., Dziewonski, A. M., Fuchs, C., & Froidevaux, C. (1987). Global digital seismographic network: Research opportunities and recent initiatives. In C. Fuchs, & C. Froidevaux, (Eds.), *Composition, structure and dynamics of the lithosphere-asthenosphere system* (Vol. 16, pp. 99–110). American Geophysical Union.

Rosa, M. L., Collaço, B., Assumpção, M., Sabbione, N., & Sánchez, G. (2016). Thin crust beneath the Chaco-Paraná Basin by surface-wave tomography. *Journal of South American Earth Sciences*, *66*, 1–14. https://doi.org/10.1016/j.jsames.2015.11.010

Ruan, Y., Lei, W., Modrak, R., Örsvuran, R., Bozdağ, E., & Tromp, J. (2019). Balancing unevenly distributed data in seismic tomography: A global adjoint tomography example. *Geophysical Journal International*, *219*(2), 1225–1236. https://doi.org/10.1093/gji/ggz356

Russo, R. (2004). *Studies of crust and upper mantle structure, mantle flow and geodynamics of the Chile Ridge subduction zone*. International Federation of Digital Seismograph Networks. https://doi.org/10.7914/SN/YJ_2004

Russo, R., Gallego, A., Comte, D., Mocanu, V., Murdie, R., & VanDecar, J. (2010a). Source-side shear wave splitting and upper mantle flow in the Chile Ridge subduction region. *Geology*, *38*(8), 707–710. https://doi.org/10.1130/G30920.1

Russo, R., VanDecar, J. C., Comte, D., Mocanu, V. I., Gallego, A., & Murdie, R. E. (2010b). Subduction of the Chile Ridge: Upper mantle structure and flow. *Geological Society of America Today*, *20*(9), 4–10. https://doi.org/10.1130/GSATG61A.1

Sandvol, E., & Brown, L. (2007). *Slip – Seismic lithospheric imaging of the Puna Plateau*. International Federation of Digital Seismograph Networks. https://doi.org/10.7914/SN/X6_2007

Santos, J. O. S. (2003). Geotectônica dos escudos das Guianas e Brasil-Central. In L. A. Bizzi, C. Schobbenhaus, J. Vidottie, & S. Conclaves (Eds.), *Geologia, tectônica e recursos minerais do Brasil* (Vol. 4, pp. 169–226). CPRM Brasília.

Santos, J. O. S., Hartmann, L. A., Gaudette, H. E., Groves, D. I., Mcnaughton, N. J., & Fletcher, I. R. (2000). A new understanding of the provinces of the Amazon Craton based on integration of field mapping and U-Pb and Sm-Nd geochronology. *Gondwana Research*, *3*(4), 453–488. https://doi.org/10.1016/S1342-937X(05)70755-3

Schimmel, M., Assumpçao, M., & VanDecar, J. (2003). Seismic velocity anomalies beneath SE Brazil from P and S wave travel time inversions. *Journal of Geophysical Research*, *108*(B4). https://doi.org/10.1029/2001jb000187

Schwartz, S. (1999). *Imaging the seismogenic zone with geodesy and seismology*. International Federation of Digital Seismograph Networks. https://doi.org/10.7914/SN/XY_1999

Schwartz, S. Y., Newman, A. N., Protti, M., & Gonzalez, V. (2009). *Nicoya Seismogenic Zone*. International Federation of Digital Seismograph Networks. https://doi.org/10.7914/SN/YZ_2009

Scripps Institution of Oceanography. (1986). *IRIS/IDA Seismic Network*. International Federation of Digital Seismograph Networks. https://doi.org/10.7914/SN/II

Silver, P., Beck, S., & Wallace, T. (1994). *Broadband study of the Altiplano and Central Andes*. International Federation of Digital Seismograph Networks. https://doi.org/10.7914/SN/XE_1994

Simmons, N. A., Myers, S. C., Johannesson, G., & Matzel, E. (2012). LLNL-G3Dv3: Global P wave tomography model for improved regional and teleseismic travel time prediction. *Journal of Geophysical Research*, *117*(B10). https://doi.org/10.1029/2012JB009525

Simões Neto, F., Julià, J., & Schimmel, M. (2019). Upper-mantle structure of the Borborema province, NE Brazil, from P-wave tomography: Implications for rheology and volcanism. *Geophysical Journal International*, *216*(1), 231–250. https://doi.org/10.1093/gji/ggy421

Sobolev, S. V., & Babeyko, A. Y. (2005). What drives orogeny in the Andes? *Geology*, *33*(8), 617–620. https://doi.org/10.1130/g21557ar.1

Takeuchi, H., & Saito, M. (1972). Seismic surface waves. *Methods in Computational Physics*, *11*, 217–295. https://doi.org/10.1016/B978-0-12-460811-5.50010-6

Tanimoto, T. (1995). Formalism for traveltime inversion with finite frequency effects. *Geophysical Journal International*, *121*(1), 103–110. https://doi.org/10.1111/j.1365-246X.1995.tb03513.x

Tape, C., Liu, Q., Maggi, A., & Tromp, J. (2009). Adjoint tomography of the southern California crust. *Science*, *325*(5943), 988–992. https://doi.org/10.1126/science.1175298

Tape, C., Liu, Q., & Tromp, J. (2007). Finite-frequency tomography using adjoint methods-Methodology and examples using membrane surface waves. *Geophysical Journal International*, *168*(3), 1105–1129. https://doi.org/10.1111/j.1365-246X.2006.03191.x

Tarantola, A. (1984). Inversion of seismic reflection data in the acoustic approximation. *Geophysics*, *49*(8), 1259–1266. https://doi.org/10.1190/1.1441754

Tassinari, C. C. G., & Macambira, M. J. B. (1999). Geochronological provinces of the Amazonian Craton. *Episodes*, *22*(3), 174–182. https://doi.org/10.18814/epiiugs/1999/v22i3/004

Tassinari, C. C. G., & Macambira, M. J. B. (2004). A evolução Tectônica do Cráton Amazônico. In V. Mantesso-Neto, A. Bartorelli, C. D. R. Carneiro, & B. B. de Brito Neves (Eds.), *Geologia do continente sul-americano-evolução da obra de fernando flávio marques de almeida*. (pp. 433–471). Beca Produções Culturais Limitada.

Teixeira, W., Cordani, U. G., Faleiros, F. M., Sato, K., Maurer, V. C., Ruiz, A. S., et al. (2020). The Rio Apa Terrane reviewed: UPb zircon geochronology and provenance studies provide paleotectonic links with a growing Proterozoic Amazonia. *Earth-Science Reviews*, *202*, 103089. https://doi.org/10.1016/j.earscirev.2020.103089

Teixeira, W., Reis, N., Bettencourt, J., Klein, E., & Oliveira, D. (2019). Intraplate Proterozoic magmatism in the amazonian craton reviewed: Geochronology, crustal tectonics and global barcode matches. In *Dyke swarms of the world: A modern perspective* (pp. 111–154). Springer. https://doi.org/10.1007/978-981-13-1666-1_4

Teixeira, W., Tassinari, C. C. G., Cordani, U. G., & Kawashita, K. (1989). A review of the geochronology of the amazonian craton: Tectonic implications. *Precambrian Research*, *42*(3–4), 213–227. https://doi.org/10.1016/0301-9268(89)90012-0

Tesoniero, A., Auer, L., Boschi, L., & Cammarano, F. (2015). Hydration of marginal basins and compositional variations within the continental lithospheric mantle inferred from a new global model of shear and compressional velocity. *Journal of Geophysical Research: Solid Earth*, *120*(11), 7789–7813. https://doi.org/10.1002/2015JB012026

Tromp, J., Tape, C., & Liu, Q. (2005). Seismic tomography, adjoint methods, time reversal and banana-doughnut kernels. *Geophysical Journal International*, *160*(1), 195–216. https://doi.org/10.1111/j.1365-246X.2004.02453.x

Universidad de Chile. (2013). *Red Sismologica Nacional*. International Federation of Digital Seismograph Networks. https://doi.org/10.7914/SN/C1

Universidad de Costa Rica. (2017). *Red Sismológica Nacional de Costa Rica (RSN: UCR-ICE)*. International Federation of Digital Seismograph Networks. https://doi.org/10.15517/TC

Universidade Federal do Rio Grande do Norte (UFRN Brazil). (2006). *Northeastern Brazil UFRN (NE Brazil)*. International Federation of Digital Seismograph Networks.

University of Brasília. (1995). *International Federation of Digital Seismograph Networks*. University of Brasilia Seismic Network.

University of Bristol (UK). (2002). *Cape Verde Mantle Structure*. International Federation of Digital Seismograph Networks.

University of Cambridge (UK) Earth Sciences. (2004). *Seismic experiment in the Aisen region of Chile (SEARCH)*. International Federation of Digital Seismograph Networks.

Universidad de Chile. (1991). *Chilean National Seismic Network*. International Federation of Digital Seismograph Networks.

University of Liverpool. (2007). *Aysen Chile aftershock deployment (ACAD)*. International Federation of Digital Seismograph Networks.

University of Oregon. (1999). *Imaging Galapagos Upwelling and Neotectonics (IGUANA)*. International Federation of Digital Seismograph Networks.

University of the West Indies Mona (Jamaica). (1985). *Jamaica Seismograph Network*. International Federation of Digital Seismograph Networks.

VanDecar, J. C., James, D. E., & Assumpção, M. (1995). Seismic evidence for a fossil mantle plume beneath South America and implications for plate driving forces. *Nature*, *378*(6552), 25–31. https://doi.org/10.1038/378025a0

Van der Lee, S. (2002). High-resolution estimates of lithospheric thickness from Missouri to Massachusetts, USA. *Earth and Planetary Science Letters*, *203*(1), 15–23. https://doi.org/10.1016/S0012-821X(02)00846-4

Van der Lee, S., James, D., & Silver, P. (2001). Upper mantle S velocity structure of central and western South America. *Journal of Geophysical Research*, *106*(B12), 30821–30834. https://doi.org/10.1029/2001JB000338

Van der Lee, S., & Nolet, G. (1997). Upper mantle S velocity structure of North America. *Journal of Geophysical Research: Solid Earth*, *102*(B10), 22815–22838. https://doi.org/10.1029/97JB01168

Van der Lee, S., Regenauer-Lieb, K., & Yuen, D. A. (2008). The role of water in connecting past and future episodes of subduction. *Earth and Planetary Science Letters*, *273*(1–2), 15–27. https://doi.org/10.1016/j.epsl.2008.04.041

Vasquez, M., Rosa-Costa, L., Silva, C., & Klein, E. (2008). *Compartimentação tectônica. Geologia e Recursos Minerais do Estado do Pará: Sistema de Informações Geográficas–SIG: Texto explicativo dos mapas geológico e tectônico e de recursos minerais do Estado do Pará. Escala, 1(1.000), 000*. Retrieved from http://rigeo.cprm.gov.br/jspui/handle/doc/10443

Vernon, F., Pavlis, G., Levander, A., & Wallace, T. (2003). *Crust-mantle interactions during continental growth and high-pressure rock exhumation at an oblique arc-continent collision zone: SE Caribbean margin*. International Federation of Digital Seismograph Networks. https://doi.org/10.7914/SN/XT_2003

Vilotte, J.-P., & RESIF. (2011). *Seismic network XS:Chile MAULE aftershock temporary experiment (RESIF-SISMOB)*. RESIF—Réseau Sismologique et géodésique Français. https://doi.org/10.15778/RESIF.XS2010

Virieux, J., & Operto, S. (2009). An overview of full-waveform inversion in exploration geophysics. *Geophysics*, *74*(6), WCC1–WCC26. https://doi.org/10.1190/1.3238367

Vlaar, N. (1989). Subduction of young lithosphere: Lithospheric doubling, a possible scenario. In Hart, S. R. & Gulen, L. (Eds.), *Crust/mantle recycling at convergence zones* (pp. 65–74). Springer. https://doi.org/10.1007/978-94-009-0895-6_7

Wagner, L., Beck, S., & Long, M. (2010). *Peru lithosphere and slab experiment*. International Federation of Digital Seismograph Networks. https://doi.org/10.7914/SN/ZD_2010

Wessel, P., Luis, J., Uieda, L., Scharroo, R., Wobbe, F., Smith, W., et al. (2019). The generic mapping tools version 6. *Geochemistry, Geophysics, Geosystems*, *20*(11), 5556–5564. https://doi.org/10.1029/2019GC008515

West, M., & Christensen, D. (2010). *Investigating the relationship between pluton growth and volcanism at two active intrusions in the central Andes*. [Data Set]. International Federation of Digital Seismograph Networks. https://doi.org/10.7914/SN/XP_2010

Wiens, D. (1997). *A broadband study of the tectonics and structure of the Antarctic Peninsula and Scotia Sea regions*. International Federation of Digital Seismograph Networks. https://doi.org/10.7914/SN/XB_1997

Wolfe, P. (1969). Convergence conditions for ascent methods. *SIAM Review*, *11*(2), 226–235. https://doi.org/10.1137/1011036

Woodward, M. J. (1992). Wave-equation tomography. *Geophysics*, *57*(1), 15–26. https://doi.org/10.1190/1.1443179

Yoshizawa, K., & Kennett, B. (2005). Sensitivity kernels for finite-frequency surface waves. *Geophysical Journal International*, *162*(3), 910–926. https://doi.org/10.1111/j.1365-246X.2005.02707.x

Yuan, Y. O., Bozdağ, E., Ciardelli, C., Gao, F., & Simons, F. J. (2020). The exponentiated phase measurement, and objective-function hybridization for adjoint waveform tomography. *Geophysical Journal International*, *221*(2), 1145–1164. https://doi.org/10.1093/gji/ggaa063

Zandt, G. (1996). *Altiplano-puna volcanic complex seismic experiment*. International Federation of Digital Seismograph Networks. https://doi.org/10.7914/SN/XH_1996

Zelt, C. A. (1998). Lateral velocity resolution from three-dimensional seismic refraction data. *Geophysical Journal International*, *135*(3), 1101–1112. https://doi.org/10.1046/j.1365-246X.1998.00695.x

Zhang, P., & Yao, H. (2017). Stepwise joint inversion of surface wave dispersion, Rayleigh wave ZH ratio, and receiver function data for 1D crustal shear wave velocity structure. *Earthquake Science*, *30*(5), 229–238. https://doi.org/10.1007/s11589-017-0197-0

Zhou, Y., Dahlen, F., & Nolet, G. (2004). Three-dimensional sensitivity kernels for surface wave observables. *Geophysical Journal International*, *158*(1), 142–168. https://doi.org/10.1111/j.1365-246X.2004.02324.x

Zhou, Y., Dahlen, F., Nolet, G., & Laske, G. (2005). Finite-frequency effects in global surface-wave tomography. *Geophysical Journal International*, *163*(3), 1087–1111. https://doi.org/10.1111/j.1365-246X.2005.02780.x

Zhou, Y., Nolet, G., Dahlen, F., & Laske, G. (2006). Global upper-mantle structure from finite-frequency surface-wave tomography. *Journal of Geophysical Research*, *111*(B4). https://doi.org/10.1029/2005JB003677

Zhu, H., Bozdağ, E., Peter, D., & Tromp, J. (2012). Structure of the European upper mantle revealed by adjoint tomography. *Nature Geoscience*, *5*(7), 493–498. https://doi.org/10.1038/ngeo1501

Zhu, H., Bozdağ, E., & Tromp, J. (2015). Seismic structure of the European upper mantle based on adjoint tomography. *Geophysical Journal International*, *201*(1), 18–52. https://doi.org/10.1093/gji/ggu492

References From the Supporting Information

Ahrens, J., Geveci, B., & Law, C. (2005). Paraview: An end-user tool for large data visualization. In C. D. Hansen, & C. R Johnson,. (Eds.), *Visualization handbook* (pp. 717–731). Butterworth-Heinemann. https://doi.org/10.1016/B978-012387582-2/50038-1

Amante, C., & Eakins, B. W. (2009). *ETOPO1 arc-minute global relief model: procedures, data sources and analysis* [NOAA Technical Memorandum NESDIS NGDC-24]. National Geophysical Data Center. https://doi.org/10.7289/V5C8276M

Clayton, R., & Engquist, B. (1977). Absorbing boundary conditions for acoustic and elastic wave equations. *Bulletin of the Seismological Society of America*, *67*(6), 1529–1540. https://doi.org/10.1785/BSSA0670061529

Durek, J. J., & Ekström, G. (1996). A radial model of anelasticity consistent with long-period surface-wave attenuation. *Bulletin of the Seismological Society of America*, *86*(1A), 144–158.

Tromp, J., Komatitsch, D., Hjörleifsdóttir, V., Liu, Q., Zhu, H., Peter, D., et al. (2010). Near real-time simulations of global CMT earthquakes. *Geophysical Journal International*, *183*(1), 381–389. https://doi.org/10.1111/j.1365-246X.2010.04734.x